Universidad de La Laguna

Master's Degree in Astrophysics

2021-2022

Unveiling the history of the Milky Way with a set of cosmological simulations from the HESTIA, MAGICC and NIHAO projects

---

Jorge Sarrato Alós

Tutors: Christopher Brook & Arianna Di Cintio

San Cristóbal de La Laguna, 2022

Abstract

Observaciones recientes desvelan más dispersión de la esperada en la metalicidad del gas del vecindario solar. Adicionalmente se han observado estrellas de metalicidad extremadamente baja en la Vía Láctea. Estos resultados discrepan con la visión que se tenía anteriormente debido a modelos de evolución química, por los que se espera que el vecindario solar sea una región bien mezclada con metalicidad altamente uniforme y similar a la del Sol. También existen observaciones recientes que apoyan la visión tradicional de un vecinadario solar bien mazclado. En caso de que se confirmen, dichos hallazgos evidencian que nuestro entendimiento de la formación de estructuras en el Universo es todavía incompleto. Debido a la complejidad y la alta variación de las escalas de los procesos involucrados en la formación de estructuras, el método predilecto para su estudio es la confección de simulaciones cosmológicas.

Tras exponer la motivación del trabajo ofrecemos una breve explicación del procedimiento general seguido en el diseño de simulaciones cosmológicas. Enumeramos los ingredientes que tienen las simulaciones y hacemos hincapié en el reto que supone la implementación de hidrodinámica para los bariones. Exponemos los dos métodos principales que se utilizan para este fin: los Lagrangianos y los Eulerianos. Señalamos las diferencias entre ambos, así como sus ventajas y desventajas sobre el otro, con especial interés en la difusión de metales. Un punto clave es la incapacidad de las simulaciones Lagrangianas para reproducir la difusión de metales, y la necesidad de implementarla añadiendo un modelo de difusión.

Utilizamos simulaciones cosmológicas hidrodinámicas de galaxias similares a la Vía Láctea de los proyectos HESTIA, MAGICC-MUGS y NIHAO para estudiar la distribución de metalicidad del gas y las estrellas del vecindario solar. La muestra de simulaciones contiene simulaciones Lagrangianas, Eulerianas, quasi-Lagrangianas (un híbrido de simulaciones Lagrangianas y Eulerianas) y una simulación Lagrangiana en la que no se ha implementado un modelo adicional de difusión. Nuestra selección de simulaciones similares a la Vía Láctea se basa en la morfología y en las masas totales y estelares de las galaxias simuladas. Durante este proceso comprobamos el acuerdo entre las masas de las galaxias simuladas y la relación masa total - masa estelar obtenida mediante el método de ”abundance matching”. Resaltamos las diferencias en los resultados de las simulaciones debidas a los distintos códigos de simulación usados por cada proyecto, y especialmente a las distintas implementaciones de la difusión de metales. Estudiamos las distribuciones de metales en las estrellas en el vecindario solar de las simulaciones mediante la confección de diagramas de [O/Fe]-[Fe/H] y de [Fe/H]-edad. Estos gráficos también son útiles para observar la presencia o falta de eventos de acreción de galaxias enanas. Comparando las características observadas en ellos con literatura sobre la Vía Láctea, identificamos cuáles de nuestras simulaciones reproducen más fielmente propiedades de nuestra galaxia. Proponemos posibles causas para las desviaciones entre algunas simulaciones y las observaciones. Resaltamos la importancia de que las galaxias simuladas sigan una historia de formación estelar similar a la de la Vía Láctea, con poca actividad de formación reciente. También destacamos la importancia de que las simulaciones sigan las relaciones de masa total - masa estelar en todo el rango de masas, desde las galaxias enanas a los candidatos de Vía Láctea.

Dos de las comparaciones con datos observacionales que realizamos son de especial importancia para la comprensión del papel que juega la difusión de metales en los resultados de las simulaciones. En primer lugar, GALAH DR3 proporciona observaciones de estrellas cercanas al

Sol. En segundo lugar, un trabajo reciente contiene medidas de la metalicidad del gas neutro del vecindario solar obtenidas mediante espectroscopia en la línea de visión hacia estrellas de tipos espectrales O y B, desvelando una notbale falta de homogeneidad en comparación con lo esperado según trabajos anteriores. Utilizamos estos datos para acotar la fuerza de la dispersión de metales que deben implementar las simulaciones cosmológicas hidrodinámicas para obtener resultados consistentes con las observaciones. Concluimos que para reproducir las observaciones mencionadas es necesario ajustar la fuerza de difusión de metales a un valor menor que el utilizado por las simulaciones quasi-Lagrangianas de HESTIA y el utilizado por las simulaciones de grupo local de NIHAO. El hecho de que otro estudio reciente apoye la visión de un vecindario solar de metalicidad altamente uniforme dificulta la obtención de conclusiones en este aspecto. Si estas úlimas se sobrepusieran a las otras, la fuerza de difusión necesaria sería mayor, pero nuestra mejor estimación seguiría siendo una fuerza de difusión similar a la usada en HESTIA.

También seleccionamos estrellas con valores de [Fe/H] notablemente menores que los del resto en el vecindario solar en las simulaciones que consideramos más adecuadas para este análisis. La presencia de estrellas de baja metalicidad en el disco es un buen indicador de la fuerza de difusión de metales en la simulación, y nos ayuda a concretar el grado necesario de difusión de metales en las simulaciones. Entender su naturaleza y procedencia podría dar lugar a avances en nuestra comprensión sobre la formación de estructuras en el Universo. Estudiamos la trayectoria de estas estrellas desde el principio hasta el final de la simulación para determinar el momento y la forma en que entraron en la Vía Láctea simulada y se formaron. Analizamos su cinemática en z = 0 y tratamos de explicarla basándonos en el origen de dichas estrellas y a sus tiempos de acreción y formación. Estudiando la galaxia simulada g15784 del proyecto MAGICC-MUGSS hallamos correlación entre el intervalo de tiempo transcurrido entre la acreción y la formación de una estrella y la tendencia de la estrella a tener dinámica similar a la del disco galáctico. No encontramos esta correlación al repetir el análisis en una simulación de NIHAO sin difusión de metales. En dicha simulación, la gran mayoría de estrellas seleccionadas tiene cinemática de disco, independientemente del resto de características estudiadas. Las limitaciones en extensión y duración del trabajo no nos permiten deducir una causa concluyente para dicha discrepancia, pero señalamos la necesidad de estudiar y comparar la historia de acreciones de ambas galaxias para comprender mejor los resultados. Hallamos que todas las estrellas seleccionadas en ambas galaxias entraron en ellas en forma de gas, antes de su formación, bien desde otra galaxia o bien directamente desde el medio intergaláctico a través de filamentos de gas. Hallamos mediante el análisis de la simulación de NIHAO sin difusión un sesgo de las estrellas de metalicidad alta frente a las de baja metalicidad para entrar en la Vía Láctea mediante la acreción desde otra galaxia y no por medio de filamentos de gas.

Contents

1. Aim of the work

Recent observations of the Milky Way (MW) show low metallicity stars (Sestito et al. [2020b]) and gas (De Cia et al. [2021]) in the local disc, which was previously unexpected. We explore cosmological simulations of Milky Way type galaxies in order to try to explain the origin of such low metallicity populations in our neighborhood.

Sestito et al. [2020b] found that very metal poor ([Fe/H]<-2.5) stars show a bias for prograde orbits and against retrograde orbits. This contradicts the general assumption that low metal stars, hypothetically accreted in mergers, would have isotropic orbits dominated by dispersion. Sestito et al. [2020a] and Santistevan et al. [2021] studied similar stars in simulations and they suggested different scenarios in which mergers would lead to them having disk-aligned orbits. They also considered the possibility that low metal stars acquire prograde orbits after in situ formation. In order to shed light on this topic, we search for low metal stars in the disks of MW-like simulations and we trace their formation and evolution throughout the simulation. Additionally, we analyze their kinematics and we determine whether if their trajectories are dominated by rotation or by dispersion.

De Cia et al. [2021] measured the chemical abundances of different regions of the interstellar medium (ISM) near the Sun via ultraviolet absorption-line spectroscopy in the line of sight (LOS) of 25 O and B stars they used as targets. The gas in the solar neighborhood was assumed to be well mixed and to have metallicities similar to that of the Sun. However, they found large variability (up to a factor ten) in the [Fe/H] values of the ISM, including regions with metallicities as low as 17 per cent of the solar value. These results must be taken with caution since they are challenged by other recent results in Esteban et al. [2022]. They use high quality metallicity determinations of tracers of the ISM composition such as Cepheids and young star clusters. They conclude the chemical composition of the ISM in the solar neighborhood is highly homogeneous. We reproduce De Cia et al. [2021]'s LOS observations, studying the feasibility of these studies in current cosmological simulations. Simulations allow us to conduct the analysis of the metallicity of the ISM gas in several regions of the galactic disk. We compare the spread of [Fe/H] values of the ISM gas towards different directions with the aforementioned LOS observations.

Only some MW-like simulations present low metallicity stars and gas as in observations. The rate at which metals are diffused in simulations is a key factor that is likely to affect the metal distribution in the galaxy and to determine the presence (or lack) of low metallicity star and gas particles. We therefore explore the effects of metal diffusion on the distribution of star and gas metallicities by studying simulations with different metal diffusion rates. We compare our findings on every simulation with each other and also with observational data from GALAH DR3 (Buder et al. [2021]). In particular, we further analyze the same simulation with and without diffusion, and a different one with metal diffusion strength lower than that of the first simulation with diffusion. We compare the results of these simulations with observations of the works cited before in order to determine which of them is in better agreement with MW observations. Based on this comparison, we look for a constraint on the metal diffusion that cosmological simulations must use for obtaining realistic results.

We present this work divided in several sections. First, in section 2 we explain the usefulness

of cosmological simulations for the study of structure formation in the Universe, and we provide general background of the field explaining the main components and types of cosmological simulations. We also list all the simulations we use for the work, together with their main characteristics: type of code used, origin of their initial conditions, their cosmology, etc. On top of simulated data, we also make use of observations, which we explain in section 3. We continue by explaining the general methodology and tools we use for the analysis of simulations in section 4. In section 4.5 we perform a general characterization of the full sample of simulated galaxies. We make a selection of 12 MW candidates based on their total mass, morphology and conformity with stellar mass - halo mass relations. We also review general traits of the stellar population of the solar neighborhood in simulations by studying [Fe/H] versus age diagrams and [O/Fe] versus [Fe/H] diagrams. We then present our main results in section 5. These are divided in two parts. In the first one we expand the previous analysis of the metal distribution of simulations by focusing on representative galaxies that use different metal diffusion implementations. In the second part we study low metallicity stars in simulations by identifying their kinematics and tracing the origin of the gas that gave place to these stars. We finally give our conclusions in section 6.

2. Cosmological simulations

2.1. Background

Cosmological simulations constitute an important tool for the prediction and study of physical phenomena in the Universe. They are specially useful for unveiling the mechanisms of formation and evolution of astronomical structures such as galaxies and galaxy clusters. These are complex processes where many multi-scale effects of different nature (dynamic, electromagnetic, etc.) play an important role. Because of its complexity and the compounded character of the involved physical processes, this problem can not be addressed analytically, and cosmological simulations are the most suitable method for learning about structure and galaxy formation. The details of these techniques have been previously reviewed by Vogelsberger et al. [2020] and Dolag et al. [2008] among others. Based on their overviews, we provide the basic description of the features and types of cosmological simulations.

Simulations must include dark matter as a key ingredient and the main driver of structure formation. Also, the presence of a dark energy component is a necessity for providing the correct expanding context where the studied processes occur. Ordinary matter is included in simulations too, as it constitutes arguably our best source of observations, and therefore it gives us the opportunity to compare our simulations with reliable observational data. Nevertheless, this component is the most challenging one when it comes to modeling its behaviour, since they do not only interact gravitationally but they also take act in hydrodynamic processes. Galaxy formation models are another essential ingredient. They play several roles of importance, such as providing descriptions for gas cooling based on its chemical abundances, for star formation, and for the injection of energy and angular momentum due to supermassive black holes and massive stars.

Cosmological simulations are carried out in the context of a Universe with a given cosmology,

which is also an ingredient of these methods. As such, cosmological simulations have also been used to test the effect of different cosmologies in structure formation and galaxy populations.

Another ingredient serves as a starting point for the simulation: the initial conditions. These describe the initial state of the simulation at a specific lookback time, and they highly influence the results. Initial conditions are extracted from observations in order to run simulations over the same map of density fluctuations that gave place to our known Universe. Overdensities are mapped in the cosmological microwave background (CMB), measured by the missions WMAP (Spergel et al. [2007]) and Planck Collaboration, which are reliable sources of data for setting the initial conditions of a cosmological simulation. All of the above, together with additional physics added in modern simulations (magnetic fields, several feedback mechanisms, etc.) and a large collection of numerical methods aimed at solving the multi-scale physical processes and improving efficiency constitute the current field of cosmological simulations.

As we already mentioned, the baryonic component constitutes an implementation challenge because it creates the need to solve hydrodynamical equations. This problem has been historically faced with two different types of methods, which creates a distinction between two different types of hydrodynamical cosmological simulations. Ones use Eulerian methods and others use Lagrangian methods. Eulerian methods are based on the division of the simulated space in a grid of cells. Then, a Riemann problem is solved for the set of hydrodynamical equations at the face of contact of each pair of cells in order to obtain fluxes and update the contribution of each cell to the conserved quantities. In general, grid-based methods suffer from limited spatial resolution, but they work well both in low and high density situations. They are also suitable for solving shocks. The value of any variable at a given point in the space and time can be straight forward approximated by the value of the variable in the cell that contains the point at an instant. However this does not work correctly in situations when discontinuities raise, such as the aforementioned hydrodynamic shocks. More correct approaches reconstruct the values of a quantity at a specific point taking into account the values at several neighboring cells and using a reconstruction function that weights each cell's value according to their distance to the point of interest. Lagrangian methods or particle methods include variants of smoothed particle hydrodynamics (SPH) methods. Their base is to discretize the simulated fluid in mass elements (particle-like) rather than volume elements. This adds inherent adaptive spatial resolution, as particles will be in average closer to each other in overdense regions than they are in underdense regions. Because of this, the resolution is lower and the method works poorly in low density regions. SPH methods do not work well either in shocked regions because they introduce spurious pressure forces on particles in regions where there are steep density gradients. These shortcomings are stressed in Agertz et al. [2007] and Shen et al. [2010] among others. Nevertheless, SPH methods are the most commonly used methods in cosmological simulations due to their adaptive resolution. The sets of equations 1 and 2 respectively show the Eulerian and Lagrangian formulations of ideal hydrodynamics. In this notation, ρ is the density, P is the pressure, $\mathbf{v}$ is the velocity vector, e is the total energy per unit mass, and $\mathrm{D}/\mathrm{Dt} \equiv \partial/\partial \mathrm{t} + \mathbf{v}\cdot\nabla$ is the Lagrangian derivative. Of course, the Lagrangian derivative is not necessary in the Eulerian implementation as the cells themselves are not moving. The set of equations 3 relates both the pressure and the total energy per unit mass with the kinetic energy per unit mass (u), and they are needed for completing the system of equations. The adiabatic index γ, usually

approached by 5/3 as for a monoatomic ideal gas, is also needed for calculating the pressure in terms of the kinetic energy per unit mass.

$$\begin{cases} \frac{\partial \rho}{\partial t} + \nabla \cdot (\rho \mathbf{v}) = 0 \\ \frac{\partial \rho v}{\partial t} + \nabla \cdot (\rho \mathbf{v} \otimes \mathbf{v} + P\mathbb{I}) = 0 \\ \frac{\partial \rho e}{\partial t} + \nabla \cdot (\rho e + P)\mathbf{v} = 0 \end{cases} \tag{1}$$

$$\begin{cases} \frac{D\rho}{Dt} = -\rho \nabla \cdot \mathbf{v} \\ \frac{D\mathbf{v}}{Dt} = -\frac{1}{\rho} \nabla P \\ \frac{e\rho}{Dt} = -\frac{1}{\rho} \nabla \cdot P\mathbf{v} \end{cases} \tag{2}$$

$$\begin{cases} e = u + \mathbf{v}^2/2 \\ P = (\gamma - 1)\rho u \end{cases} \tag{3}$$

Shen et al. [2010] also studied how entropy diffusion occurs in both Eulerian and SPH cosmological simulations. They showed again that Eulerian simulations produce more physically correct results for the evolution of a buoyant gas bubble and gas in a galaxy cluster. The hypothesized cause for SPH simulations failing in these scenarios is that they lack of a diffusive term to mix entropy and heat. This means that tracers in SPH simulations, such as metals, are not mixed as well. Metals in simulations highly influence the evolution of galaxies, controlling gas cooling and therefore affecting star formation. Along with metal returns via supernovae, stellar wind and others, metal mixing determines the distribution of different chemical elements throughout the simulation. For this reason, correctly modelling metal diffusion is a need for accurate cosmological simulations. SPH methods deal with this issue by adding diffusion into the code. For example, Wadsley et al. [2008] were able to match the results of Eulerian simulations by adding a diffusion rate D to SPH simulations, which depends on the pairwise velocity Δv and on the resolution scale h_{SPH}, with a constant diffusion coefficient C typically of the order of $\sim$ 0.05-0.1. This rate controls the variation of a scalar quantity A over time due to diffusion as described in equation 5.

$$D = C\Delta v h_{SPH} \tag{4}$$

$$\frac{dA}{dt}|_{Diff} = \nabla (D \nabla A) \tag{5}$$

2.2. Simulations used

2.2.1. HESTIA

Local group simulations of the "High-resolutions Environmental Simulations of The Immediate Area" project (HESTIA, Libeskind et al. [2020]) use their own set of initial conditions obtained from peculiar velocities data in the CosmicFlows-2 catalogue (Tully et al. [2013]) and in agreement with ΛCDM theory. The cosmology of these simultaions is described by the following

parameters: H_0 = 100h km s^{-1} Mpc^{-1} with h = 0.677, Ω_m = 0.270, Ω_Λ = 0.682, Ω_b = 0.048 and σ_8 = 0.83.

HESTIA simulations are computed with the AREPO code (Springel [2010], Pakmor et al. [2015]), which uses a moving, shape-adapting mesh to solve the ideal magntetohydrodynamics (MHD) equations. The mesh is allowed to move rather than being fixed as in conventional Eulerian simulations. This results in a quasi-lagrangian simulation that combines pure Lagrangian and Eulerian features. They also make use of the Auriga galaxy formation model (Grand et al. [2017]). Due to their hybrid nature, HESTIA simulations have Eulerian-like implicit metal diffusion between cells, and there is no need for a sub-grid model implementation that accounts for this mixing phenomenon. There is however a difference in the strength of diffusion with respect to pure Eulerian methods: since the cells move along with the fluid, the velocity flows in each cell are modified, causing a general decrease in metal (and other tracers) mixing. Thus, intuitively, quasi-lagrangian methods have diffusion strengths between those of pure Eulerian and pure Lagrangian methods.

HESTIA consists in three different simulations. They contain MW-like and M31 galaxies in addition to dwarf galaxies as we observe in the Local Group. For the current study we will only use the galaxies corresponding to the two most massive halos, as they are the ones that potentially resemble the MW. This makes a total of 6 galaxies of interest from the HESTIA project.

2.2.2. MAGICC-MUGS

We use the galaxy g15784 from the McMaster Unbiased Galaxy Simulations (MUGS, Stinson et al. [2010]). The simulation is based on initial conditions from a realization of the CMBFAST (Seljak and Zaldarriaga [1996]) and it makes use of the GASOLINE SPH code in order to evolve over time. Diffusion is additionally implemented over the SPH routine according to Wadsley et al. [2008] with a diffusion coefficient (C in equation 4) of 0.05.

The cosmology adopted for the MAGICC project is that of the Wilkinson Microwave Anisotropy Probe (WMAP, Spergel et al. [2007]): H_0 = 100h km s^{-1} Mpc^{-1} with h = 0.73, Ω_m = 0.24, Ω_Λ = 0.76, Ω_b = 0.04 and σ_8 = 0.76.

2.2.3. NIHAO - individual galaxies

The project "Numerical Investigation of a Hundred Astrophysical Objects" (NIHAO, Wang et al. [2015]) consists in a set of 100 cosmological hydrodynamical simulations performed using the ESF-GASOLINE2 SPH code (a modified version of the GASOLINE N-body SPH solver described in Wadsley et al. [2004]). We make use of 12 of these galaxies.

The simulated galaxies were selected from previous large scale simulations (e.g. Dutton and Macciò [2014]) and the initial conditions for simulations were created using a modified version of the grafic2 package (Bertschinger [2001]).

The cosmology adopted for the NIHAO project uses the following set of parmeters: H_0 = 100h km s^{-1} Mpc^{-1} with h = 0.671, Ω_m = 0.3175, Ω_Λ = 0.6824, Ω_b = 0.049 and σ_8 = 0.8344.

As a SPH project, NIHAO makes use of a metal mixing model over the general GASOLINE code to correctly model this phenomenon. Shen et al. [2010] implemented this feature in gasoline using a formulation that differs from that described in Wadsley et al. [2008] in that it

makes use of a turbulent mixing model rather than calculating diffusion rates from pairwise velocities alone. Their diffusion rates are calculated as in 6, where S_{ij} is the so called trace-free shear tensor.

$$D = C \mid S_{ij} \mid h^2_{SPH} \tag{6}$$

The diffusion coefficient (C in equation 6) is set to 0.05 just like for MAGICC, but note that they use different metal diffusion models. Although Shen et al. [2010]'s model intends to match the results of Eulerian simulations just like Wadsley et al. [2008]'s, the differences in the implementations can lead to unequal metal diffusion efficiencies even if the same diffusion coefficient is used.

2.2.4. NIHAO - Local group

These simulations (Arora et al. [2021]) use the same code and cosmology as in the NIHAO project, but the initial conditions are extracted from the Constrained Local UniversE Simulations (CLUES, Gottlöber et al. [2010]) project. They contain MW, M31-like galaxies and their associated dwarfs in a cosmological box of side 100 Mpc h^{-1}.

Two different suites of simulations are available, as described in the original paper: a first one with metal diffusion (md) from Shen et al. [2010] and a second one with no metal diffusion at all (nmd). The Initial Mass Function (IMF) used is Chabrier's (Chabrier [2003]). Each set of simulations contains two main halos with total mass $M_{200} \sim 10^{12} M_\odot$. More detailed information on these simulations can be found in section 2.2 of Arora et al. [2021].

Just like in HESTIA simulations, we are only interested in the two most massive galaxies in the simulations in order to compare with MW observations. Taking into account both suites (with and without metal diffusion), we will study 4 galaxies from NIHAO-LG simulations.

3. Observational data: GALAH DR3

The GALactic Archaeology with HERMES (GALAH, Buder et al. [2021]) survey is a Large Observing Program using the HERMES (Raskin et al. [2010]) instrument with the Anglo-Australian Telescope. The aim of the survey is to obtain the highest spectral resolution multi-dimensional datasets for over a million stars of all ages and locations in the Milky Way to trace the full history of the Galaxy. This data is highly relevant for the study of the formation and evolution of the MW and other galaxies. The third data release of the survey was published in November 2020, and it comprises of data for 588571 nearby stars (81.2% of them are within 2 kpc from the Earth), out of which 65% are classified as giants, 34% as dwarfs and the remaining 1% remains unclassified.

Out of the several fields of data they provide for each individual galaxy, we use their spatial coordinates, specially their galactocentric radius values, and their chemical abundances of iron, oxygen and hydrogen. This data is all we need to make our study on the distribution of metals of the stars in the solar neighborhood.

4. Methods

In this section, we explain the tools and numerical methods used in order to analyze our simulations, in particular in order to select MW halos, identify their stars around the solar neighborhood, compute their metallicty and make further analysis.

4.1. Halo finder

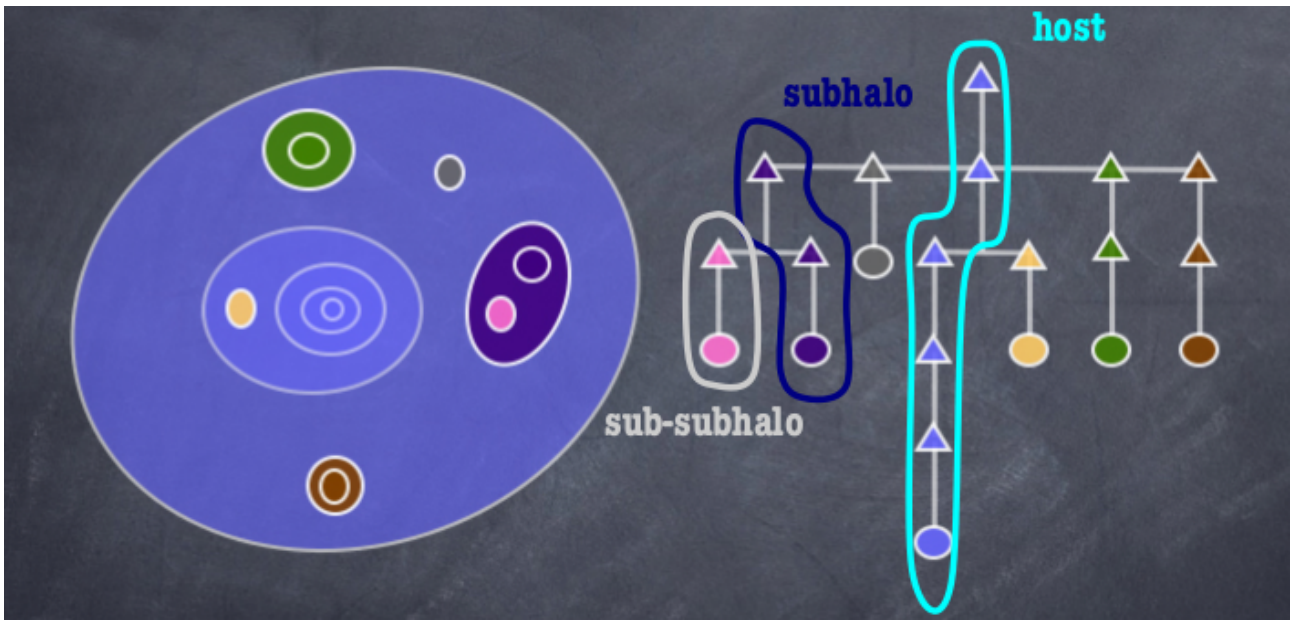

Figure 1: Left: Representation of hypothetical halos identified by AHF. Elliptical contours mark isodensity regions. Right: tree organization of halos showed in the left side of the figure. Source: AHF user's guide.

A halo finder is a program used for the analysis of cosmological simulations. It has the ability to identify sets of gravitationally bound particles as those in a particular halo. This is done mainly by identifying iso-density contours, and the selections are then refined with other techniques such as iteratively calculating the graviational potential ϕ experimented by a particle, and comparing its velocity with the escape velocity $v_{esc} = \sqrt{2\,|\,\phi\,|}$. The halo finder retrieves the halo centres, organizes the halos and sub-halos in a tree structure and obtains several halo properties of interest such as total mass, gas mass, stellar mass, virial radius, velocity dispersion, parent halo, etc. Running a halo finder is extremely advisable for easing the analysis of a simulation. In this work we use Amiga's Halo Finder (AHF, Knollmann and Knebe [2009])

4.2. Pynbody

The data of each individual simulation is stored in several files known as snapshots. These files contain the state of the simulation at a given instant (either referred to as time from the start, lookback time or redshift). Inside the snapshot files we find information about several types or families of particles. The main ones are stars, gas and dark matter. Additionally, other families such as stellar winds may be included.

Due to their use of the Auriga code rather than Gasoline's, HESTIA simulations exhibit particularities in the data stored in their snapshots when compared to MAGICC or NIHAO.

We analyze the simulations using the python package pynbody. It allows us to read and process data from the snapshots. The first steps after loading the data of a snapshot are centering the coordinate system in the halo we want to study and aligning it correctly. The most common alignments are face on, so the disk of the galaxy (if it has a disk) lays in the XY plane and edge on or side on, so that the hypothetical disk lays in the XZ plane. These are accomplished by maximizing the angular momentum distribution with respect to a given axis (Z and Y respectively). Pynbody also has the function of generating rendered images of simulations by determining the radiation fluxes emitted by gas and stars in each passband from their temperature and metallicity. Side on renders are specially important when looking for simulated galaxies that resemble the MW in morphology, as they show us whether if the galaxy presents a disk or not.

For the pynbody package to correctly read HESTIA data, we made slight changes to the reading module, since AURIGA's format was not completely supported.

Once the data is read and the reference system is properly set up, we can proceed with the analysis, for which we use several particle properties stored in the snapshots:

- IDs: each particle (of any kind) has an unique identifier number which allows us to distinguish it from any other. These IDs are the same for a given particle in every snapshot except in the case of HESTIA simulations, where they can not be used to track particles at different times throughout the simulation.
- Positions and velocities of any particle in the simulations: both in a cartesian reference system and in a cylindrical reference system.
- Mass fractions of several chemical elements. We are mainly interested in hydrogen, oxygen and iron.
- Age: time passed since the formation of a star.

We study the state of galaxies in the last snapshot of the simulations, at z = 0. We only use the rest of the snapshots for tracking the formation and evolution of stars we are interested in.

4.3. Selecting the Solar neighborhood

The solar neighborhood is defined as a region that spans typically ~1-2 kpc radially from the Sun. Thus, selecting this region of the MW is straight-forward if we know the coordinates of both the Sun and each other star/gas particle of interest. Simulations, however, do not contain a specific star particle to be considered as the Sun of the MW. Therefore, there are infinite potential Sun locations at a ring of ~8 kpc radius from the center of the galaxy roughly centered in the galactic plane, which we call the solar annulus. From there, an approximation for the selection of all particles in the "solar neighborhood" is imposing hard limits between ~ 6 kpc and 10 kpc for galactocentric radii and between -2 kpc and 2 kpc for the vertical coordinate over the galactic plane. For many purposes this simple selection is sufficient, and it will hold during the work unless we indicate the contrary. However, when comparing with specific data sets, a comparison is better made by using selection methods which best mimic that observed data. Therefore, when comparing with GALAH data (as in section 5.3), we decided to improve the radial selection in order to reproduce its distribution of galactocentric radius values. This makes our results more correctly comparable with observations and it also assures they are

representative of the solar region, avoiding the inner zone of the galactic disk to dominate due to its greater stellar density. Note we ignored other factors affecting the selection function of GALAH DR3.

From a practical viewpoint, the radial selection is carried out as follows: we make a histogram of the cylindrical galactocentric radius of stars in GALAH DR3 with 100 bins (a different choice would modify the result slightly), we interpolate over the full range of radii obtaining a continuous function f and we normalize the maximum value to 1. This function of radii is shown in figure 2. Then we select all the stars included between the minimum and maximum radial coordinates of GALAH data. For each star, we generate a random number between 0 and 1 from an uniform distribution, and if this number is greater than the value of f for the star's radius, then the star is dropped from the selection.

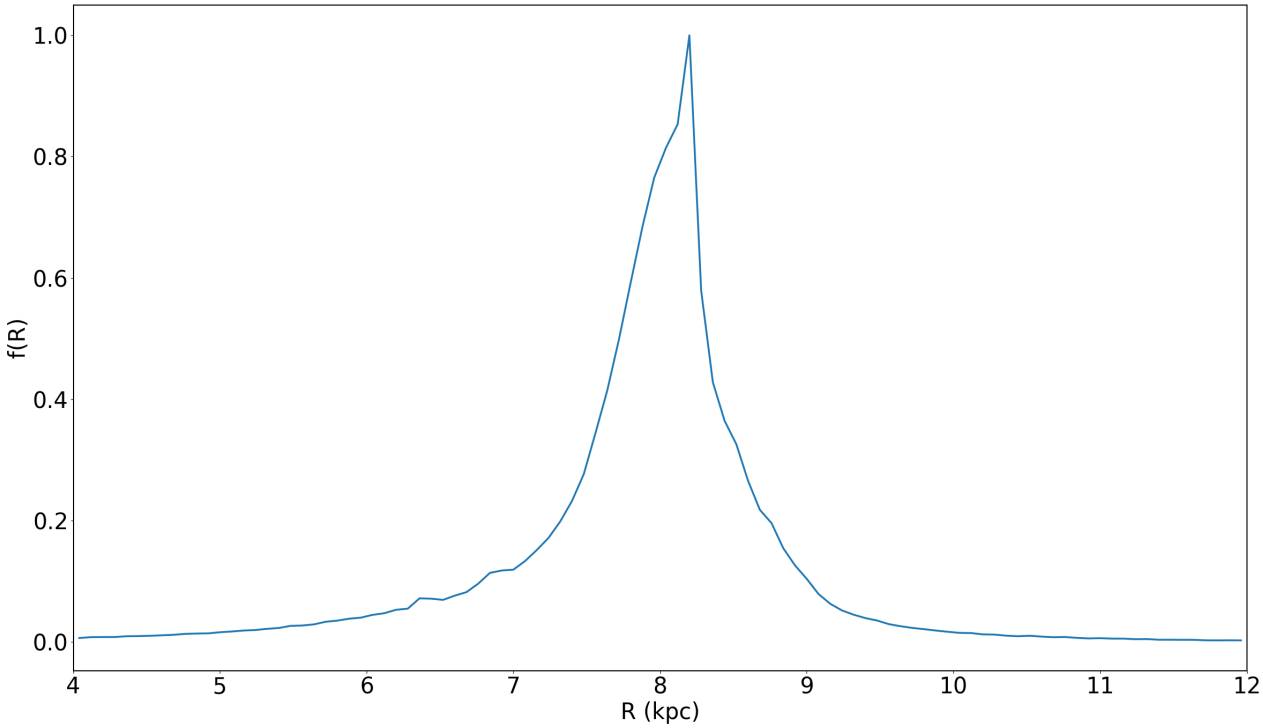

Figure 2: Normalized interpolated distribution of cylindrical galactocentric radii in GALAH DR3.

4.4. Transformation of metal abundances data

This study is conducted using common logarithms of abundances with respect to solar quantities (e.g [Fe/H], [O/Fe]). Since the quantities stored in the simulated data are chemical abundances, we need to relate both variables with each other. In order to calculate the common logarithm of an element A over another B with respect to solar quantities we use the following definition:

$$[A/B] = \log\left(\frac{X_A}{X_B}\right)_* - \log\left(\frac{X_A}{X_B}\right)_\odot$$

Where X_E is the mass fraction of an element E. Since we are mainly interested in [Fe/H] and [O/Fe], we need ratios between the mass fractions of those elements in the Sun. We use data from Anders and Grevesse [1989]:

$$\left.\frac{X_{\rm Fe}}{X_{\rm H}}\right|_{\odot} = 0.00125/0.706 \quad ; \quad \left.\frac{X_{\rm Fe}}{X_{\rm H}}\right|_{\odot} = 84/12.5$$

4.5. Identifying MW candidates

The following table gives a short overview of the general characteristics of the galaxies considered in this study.

Table 1: General properties of the simulated galaxies.

Name	Project	Total mass (10^{12} $M_\odot$)	Gas mass (10^{11} $M_\odot$)	Star mass (10^{10} $M_\odot$)	Rvir (kpc)	Number of particles
g15784	MAGICC-MUGS	1.51	1.35	8.28	241.99	5.60×10^6
g2.79e12	NIHAO	2.37	1.35	13.46	216.69	4.02×10^6
g1.92e12	NIHAO	1.57	0.681	10.67	189.12	3.62×10^6
g1.77e12	NIHAO	1.49	0.762	9.28	185.68	1.98×10^6
g1.12e12	NIHAO	0.749	0.378	5.32	147.66	1.28×10^6
g8.28e11	NIHAO	0.782	0.805	1.26	149.80	1.51×10^6
g8.26e11	NIHAO	0.685	0.497	3.18	143.34	1.70×10^6
g8.13e11	NIHAO	0.665	0.312	4.51	141.92	1.37×10^6
g8.06e11	NIHAO	0.633	0.421	3.02	139.61	1.53×10^6
g7.66e11	NIHAO	0.624	0.272	4.00	138.95	1.19×10^6
g7.55e11	NIHAO	0.599	0.473	2.12	137.11	1.29×10^6
g7.44e11	NIHAO	0.789	0.808	1.31	150.26	1.10×10^6
g7.08e11	NIHAO	0.541	0.400	2.10	132.51	3.98×10^6
mdh1	NIHAO-LG	1.80	0.507	3.49	197.99	1.71×10^6
mdh2	NIHAO-LG	0.655	0.401	3.76	141.24	1.68×10^6
nmdh1	NIHAO-LG	0.661	0.523	3.17	141.66	1.60×10^6
nmdh2	NIHAO-LG	1.80	0.668	2.62	198.00	1.57×10^6
09_18h1	HESTIA	2.35	1.16	9.88	216.19	2.67×10^7
09_18h2	HESTIA	1.44	1.03	8.97	183.68	1.89×10^7
37_11h1	HESTIA	0.705	0.540	3.80	144.76	8.95×10^6
37_11h2	HESTIA	0.691	0.404	4.06	143.74	8.58×10^6
17_11h1	HESTIA	3.78	2.66	22.14	253.33	2.40×10^7
17_11h2	HESTIA	1.56	1.14	8.85	188.53	2.00×10^7

The full set of simulations comprises of galaxies with total masses ranging from 5.41×10^{11} $M_\odot$ through 3.78×10^{12} $M_\odot$. We also observe variability in the stellar mass values of the MW candidates. Stellar masses of galaxies and total masses of their halos have previously related to each other via the abundance matching approach. This technique consists in matching the observed distribution of stellar masses of galaxies and the distributions of total masses of halos found in simulations under the assumption that the most massive galaxy will lay in the most massive halo and so on. Moster et al. [2012] and Kravtsov et al. [2018] among others provide a parametric form of this relation. We plot the aforementioned relations together with the masses of our galaxies in order to check if they agree with the observed trends. Aside from using the usual abundance matching method, Kravtsov et al. [2018] provide a stellar mass - halo mass relation obtained through scattered abundance matching. This approach includes a fixed scatter described by a log-normal probability distribution function in the abundance

matching process, in such a way that the most massive galaxy is not directly assumed to lay in the most massive halo, but in one within a certain range of masses centered in the mass of said halo. In figure 3 we see that the stellar mass - halo mass relations we consider give similar results in the range of masses that we are assessing. We only plot Kravtsov et al. [2018]'s relation with dispersion since the version without dispersion is very similar to this one, and Moster et al. [2012]'s relation already serves the purpose of a stellar mass - halo mass relation with no dispersion. We find our galaxies to be in best agreement with the trend of Kravtsov et al. [2018]'s abundance matching relation, which is steeper than Moster et al. [2012]'s at the high mass end. Most of our galaxies present higher stellar masses than those predicted by abundance matching stellar mass - halo mass relations. Kravtsov et al. [2018] does not provide estimates for the uncertainties of their abundance matching stellar mass - halo mass relations. However, based on the orders of magnitude of the uncertainties of Moster et al. [2012]'s relation, we consider the dispersion among our galaxies to be within normality. Galaxies g8.28e11 and g7.44e11 have the lowest stellar masses among our sample, and they are also the ones that deviate the most from stellar mass - halo mass relations, together with the most massive galaxy (both in terms of stellar and total mass) 17_11h1.

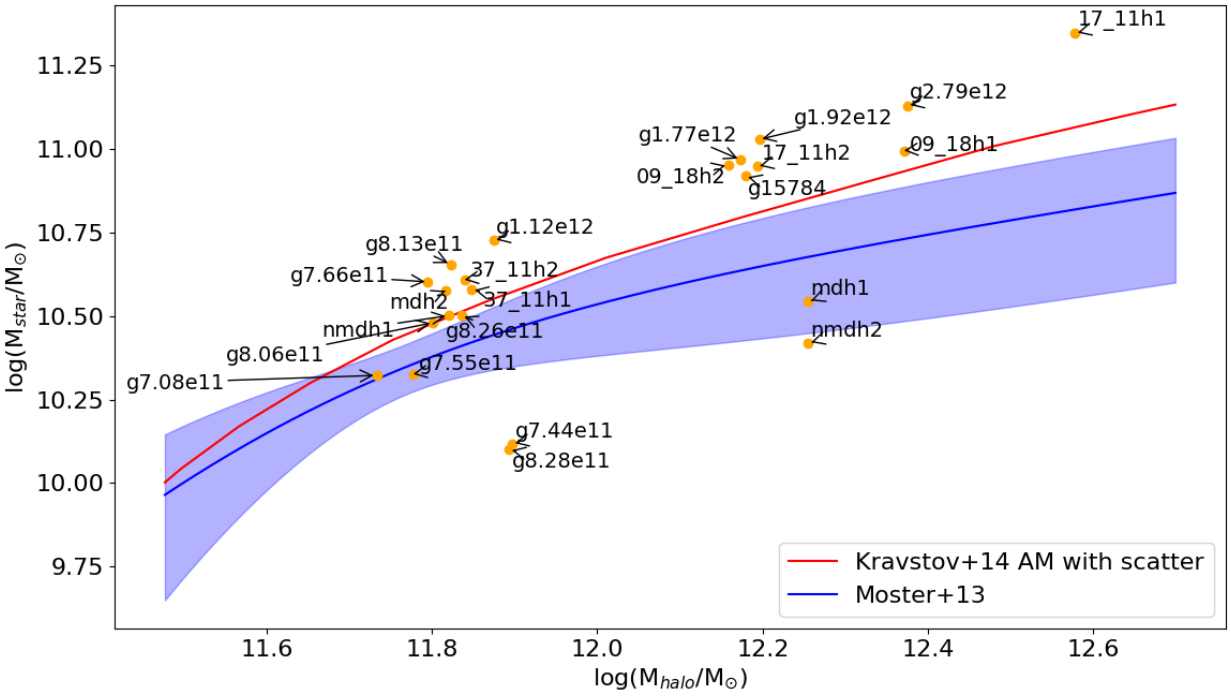

Figure 3: Stellar mass versus halo mass. Orange dots mark the positions of our simulated MW candidates. They are labeled and indicated with arrows. Moster et al. [2012]'s abundance matching relation is plotted in blue with a shadowed region of the same color indicating its uncertainty at 1σ. Kravtsov et al. [2018]'s abundance matching relation with scatter is represented by the red solid line.

The Milky Way is a spiral galaxy with a total mass of around 10^{12} $M_\odot$ (McMillan [2011], Kafle et al. [2012], Kafle et al. [2014],McMillan [2016] among others) and stellar mass of $\sim 5\times10^{10}$ $M_\odot$ (e.g. McMillan [2011],Licquia and Newman [2015a],Licquia and Newman [2015b]). Measuring the total mass of our own galaxy is a challenge that still produces discussion among scientists. A variety of methods have been used for this end, yielding results over a wide range of masses, as

shown in figure 4 from Callingham et al. [2019]. There are even more estimations of the total mass of the MW in the literature that are not shown in said figure e.g. virial mass of $0.8^{+1.2}_{-0.2}\times10^{12}$ $M_\odot$ from Battaglia et al. [2005] and virial mass of $1.51^{+0.45}_{-0.4}\times10^{12}$ $M_\odot$ from Fritz et al. [2020].

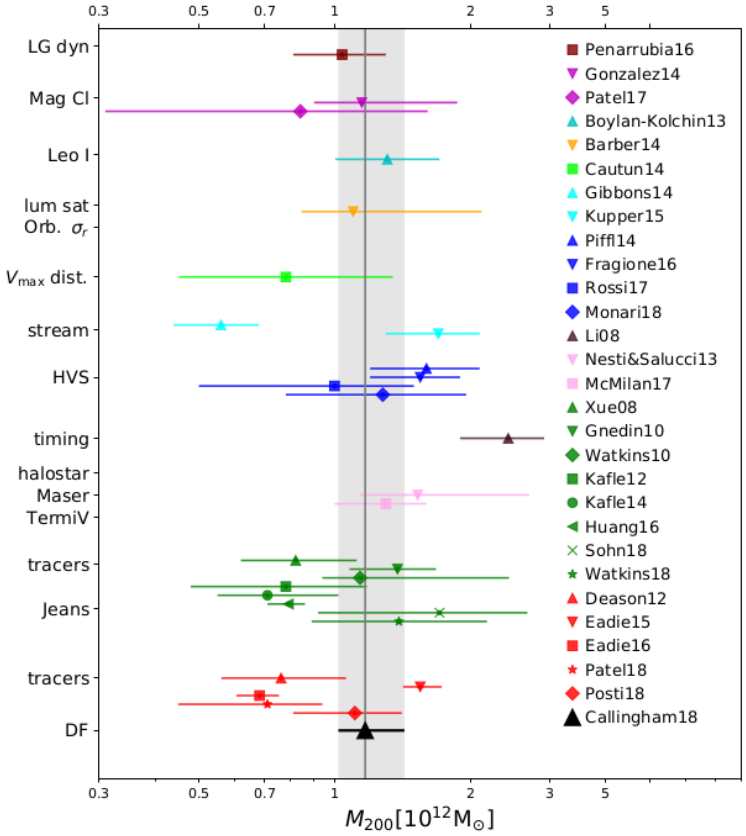

Figure 4: Source: Callingham et al. [2019]. Comparison of their inferred MW halo mass with a selection of previous estimates. The vertical line and the shaded region show their M 200 estimate and its 68% confidence limit. The remaining symbols show previous estimates (see legend), with the horizontal lines corresponding to the quoted 68% confidence limits. The results are grouped according to the methodology employed (see vertical axis). In the horizontal axis is M 200 , the mass contained within R 200 (the radius enclosing a mean density equal to 200 times the critical density). Some of the previous estimates were converted to M 200 by assuming an NFW profile and the mean concentration predicted for that mass.

We check the total masses of our candidate galaxies which are stored in the AHF data table (see table 1) and discard the ones which deviate too much from observations. Despite the wide range of total mass estimations in the literature (see figure 4), we choose to be more restrictive in the selection, keeping galaxies roughly between 0.7 and 1.5 $\times10^{12}M_\odot$. We also do not discard galaxies with masses that we consider to be too close to these limits, so the definitive limits of our selection after adding the slightly off-limits galaxies are 0.685 and 1.56 $\times10^{12}M_\odot$. Galaxies mdh1 and nmdh2 of total mass $1.8\times10^{12}M_\odot$ are exempt from this discarding process because they constitute an essential source of data for our study of the impact of metal mixing in the evolution of MW-like galaxies. Based on the stated above we discard: g2.79e12, g8.13e11, g8.06e11, g7.66e11, g7.55e11, g7.08e11, mdh2, nmdh1, 09_18h1, 17_11h1. Since figure 3 shows our galaxies to be in general agreement with stellar mass - halo mass relations, we do not consider it necessary to discard any galaxies based on their stellar mass values after the total mass filtering we just performed.

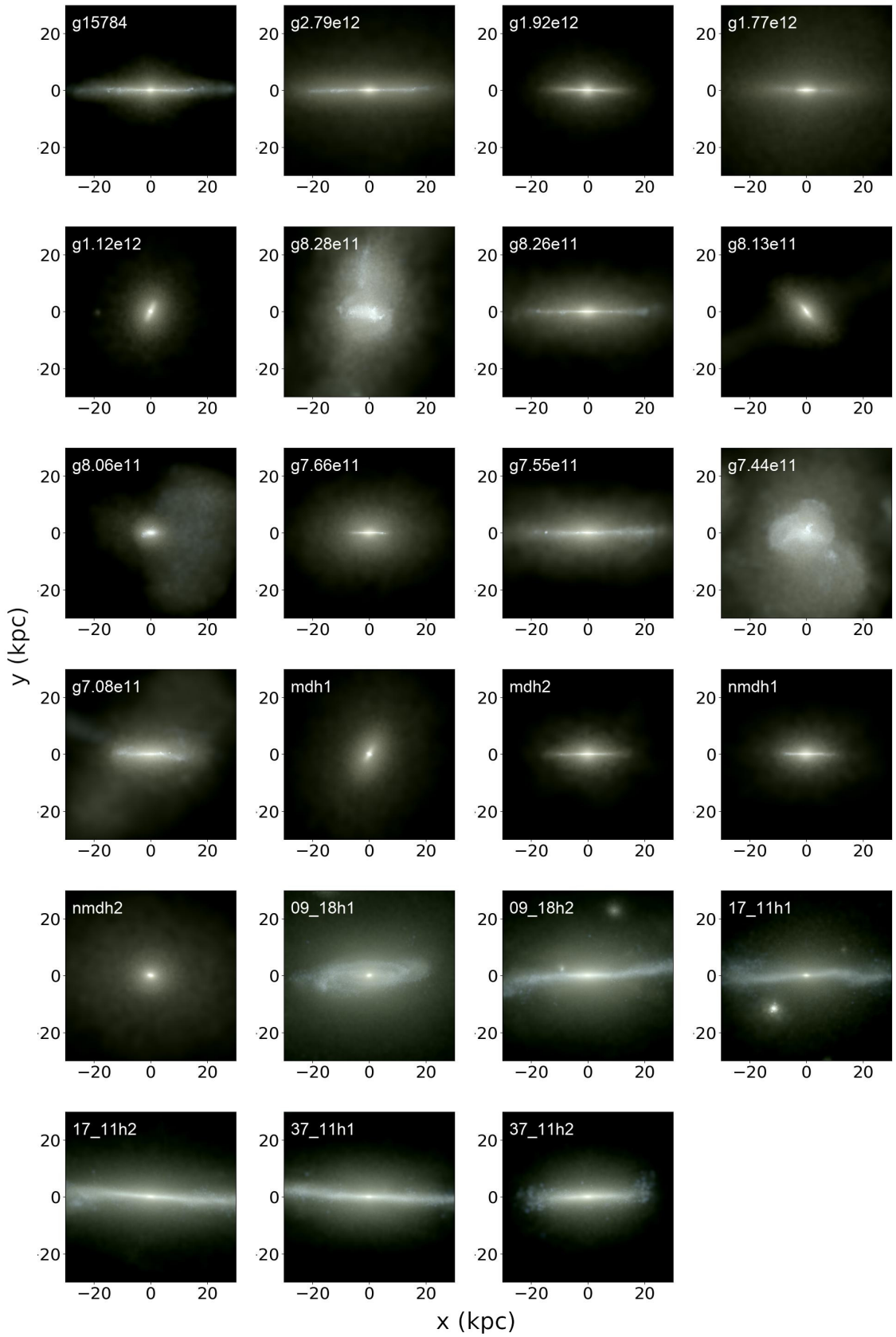

Figure 5: Side on projections used to check similitude of the simulated galaxies with the MW. Renders use Sloan's passbands r, v and b for RGB channels of the image respectively, except for HESTIA, where i, r and g are used instead.

To visualize the morphology of MW candidates, side on renders of the candidate galaxies are shown in figure 5. Visual inspection of this figure allows us to discard the following candidates due to the clear lack of a disk: g7.44e11, g8.06e11, g8.13e11, g8.28e11, g1.12e12, n10.0_e0.13_nmdh2, and n10.0_e0.13h1.

As a result, the remaining candidates are: g15784, g1.92e12, g1.77e12, g8.28e11, g8.26e11, g7.44e11, mdh1, nmdh2, 09_18h2, 37_11h1, 37_11h2 and 17_11h2.

Our galaxy has a specific metal distribution which we have been able to measure. In the solar neighborhood region, the [α/Fe] versus [Fe/H] plane of this distribution shows a characteristic shape with an elbow where the slope of the relation changes. Another interesting feature is the presence of two peaks of density of stars in the plane separated by a gap. Hayden et al. [2015] used APOGEE data (Majewski et al. [2017]) to examine the [α/Fe] versus [Fe/H] plane and to study the nature of the peaks using figure 6. The third panel of the top and middle rows show the features described above for the solar neighborhood. They found each peak to be associated with different stellar populations that are also spatially separated in the galaxy. Note since oxygen is so abundant among α particles, the [O/Fe] common logarithm is very similar to [α/Fe]. Thus, we consider the [O/Fe] versus [Fe/H] planes of the simulated galaxies are comparable to the results of Hayden et al. [2015] and we will use them during our anlysis.

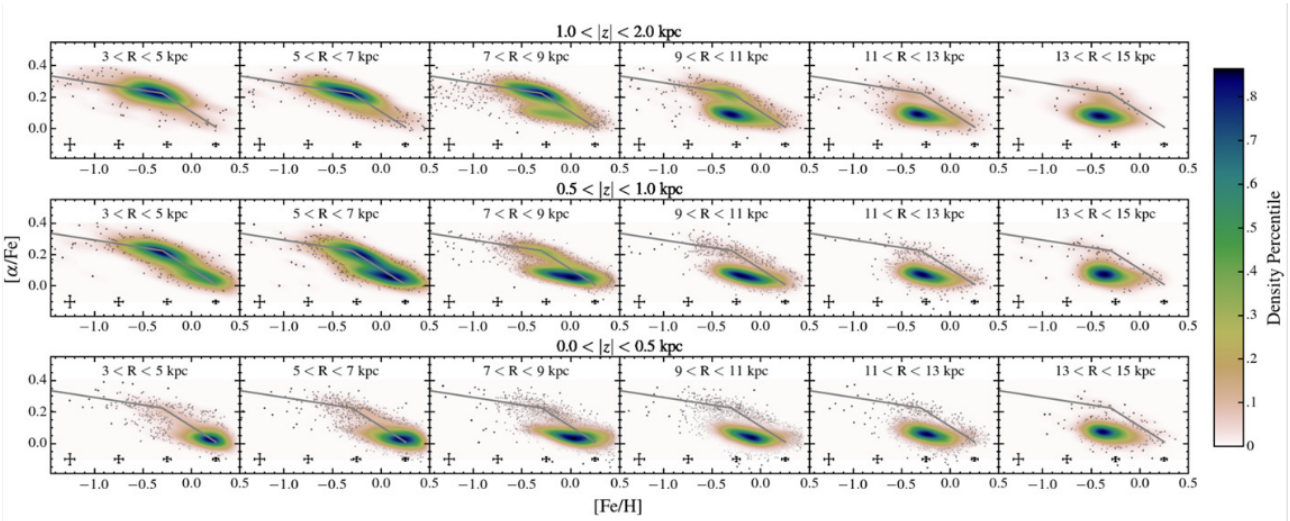

Figure 6: Source: Hayden et al. [2015]. Stellar distribution of MW stars in the [α/Fe] vs. [Fe/H] plane as a function of R and |z |. The typical uncertainty in the abundances is shown as a function of metallicity across the bottom of each panel. The size of individual points is inversely related to the density at that location, to avoid saturation. Top: observed [α/Fe] vs. [Fe/H] distribution for stars with 1.0 < |z |< 2.0 kpc. Middle: observed [α/Fe] vs. [Fe/H] distribution for stars with 0.5 < |z |< 1.0 kpc. Bottom: observed [α/Fe] vs. [Fe/H] distribution for stars with 0.0 < |z |< 0.5 kpc. The gray line on each panel is the same, showing the similarity of the shape of the high-[α/Fe] sequence with R. The extended solar-[α/Fe] sequence observed in the solar neighborhood is not present in the inner disk (R < 5 kpc), where a single sequence starting at high [α/Fe] and low metallicity and ending at solar [α/Fe] and high metallicity fits our observations. In the outer disk (R > 11 kpc), there are very few high-[α/Fe] stars

Ideally, a simulated MW-like galaxy should have similar mass to that observed for our galaxy, similar morphology, metal distribution, velocity dispersion, etc. We make increasingly strict restrictions, first focusing on filtering on the values of total and stellar mass and specially on the observed morphology of candidates. We keep the selected galaxies based on these restrictions

for the general analysis of the sample. Later we narrow the selection by looking at the chemical distribution of the galaxies for conducting more specific studies.

5. Results

5.1. [Fe/H] versus age diagram

We show the [Fe/H] versus age plane of stars in the solar neighborhood of the seleccted MW candidates (see figure 7). Note the ages of stars in the X-axis also serve as a lookback time variable for the simulation. These plots are useful for characterizing the [Fe/H] distribution of the stellar population in the vicinity of the solar region and for studying the merger history of the galaxy.

We see for all galaxies a clear main sequence in the plane, which represents the stars that were formed inside the main galaxy. We notice large variability in the spread of these main sequences. NIHAO galaxies have the thinnest main sequences possibly due to their efforts to reproduce Eulerian metal mixing, which is the strongest over all the simulation schemes. This homogenizes the [Fe/H] values of stars, and it restricts the spread on Y-axis of the diagram for young stars born from gas that has been through longer times of metal mixing interactions. The galaxy g15784 from MAGICC also uses a sub-grid model for metal diffusion to match the results of Eulerian simulations, but it shows slightly more spread on [Fe/H] than NIHAO galaxies. Even if both NIHAO and MAGICC simulations use the same diffusion coefficient of 0.05, the differences in their diffusion models could be the reason of the seeming discrepancy. Since we only study one MAGICC galaxy, this may as well be only a statistical deviation. HESTIA galaxies show even more dispersion, being consistent with their quasi-Lagrangian scheme, whose metal mixing is not as strong as the one produced by Eulerian methods. The galaxy nmdh2 is an exception among NIHAO galaxies, since its metal mixing sub-grid model is inactive and SPH methods alone are unable to reproduce its effects. For this reason, it is consistent that this galaxy shows the most spread in the diagram when compared to the rest. The broadness of the main sequence in HESTIA simulations is comparable with that of nmdh2, but the bulk of stars is highly more concentrated as shown by the red color areas. The densest contours of nmdh2's diagram span over a wider region of the [Fe/H]-age plane than those seen in HESTIA panels. Aside from differences in the treatment of metal diffusion, galaxies g8.28e11 and g7.44e11 show other particularities: their main sequences are the thinnest out of all NIHAO individual galaxy simulations, and their peak of stars in the diagram is shifted to very young ages compared to the rest of simulations. HESTIA's galaxy 09_18h2 also presents a peak of stars of low ages, although the ones of the aforementioned NIHAO galaxies are more concentrated in the plane.

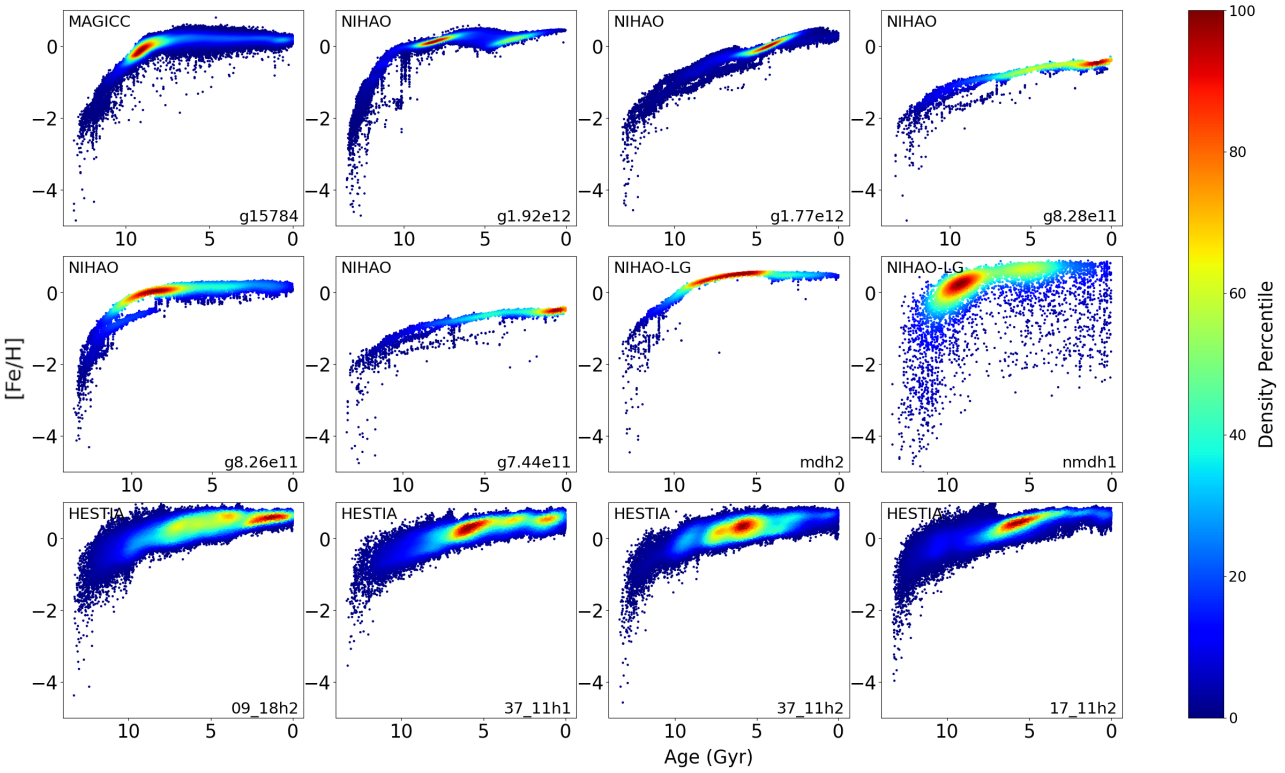

Figure 7: [Fe/H] versus age diagrams of the stars in the solar neighborhood of the selected galaxies.

Apart from the main sequences that we ascribe to the MW-like galaxy, we notice thinner sequences of stars that end up merging into the main one at some point of the simulation. We attribute these components to smaller galaxies that were accreted into the main halo during their evolution. We also note the lack of these tracks of stars in HESTIA and nmdh2 diagrams. The stars of accreted galaxies constitute the secondary sequences of the diagram, and the thinner sequences' paths in the diagram stop and collapse into the main sequence at the time of accretion. These events trigger star formation, generating groups of stars of similar ages. An example can be seen in galaxy g1.92e12 at the age (lookback time) of roughly 10Gyr. As we mentioned, we can not distinguish secondary sequences of accreted galaxies in the nmdh2 diagram. Given the more than reasonable hypothesis that mergers are still occurring, we conclude that the stars from accreted galaxies are mixed in the diagram with those of the main galaxy. This is expected since the lack of metal mixing prevents the homogenization of star metallicities in each galaxy. HESTIA simulations, however, do model metal mixing even if its strength is lower than that of pure Eulerian simulations, and we still do not see separation between stars from accreted galaxies and the main galaxy in the [Fe/H] versus age diagram. In order to study this fact, we extend the stellar mass - halo mass relation represented in figure 3 to lower masses, and we include the dwarf halos in NIHAO and HESTIA LG simulations (see figure 8). We find HESTIA galaxies to be more spread than NIHAO's in the stellar mass - halo mass plane. This is expected since we are plotting three different HESTIA LG simulations, and only two from NIHAO, which only differ from each other in their treatment of metal mixing, so they do not show great differences in masses. NIHAO galaxies clearly follow observational stellar mass - halo mass relations with more precision than HESTIA's. The latter present a general excess of stellar mass for a given halo mass. This is specially noticeable for halos in the range of $\sim 9.5 < \log(M_{\rm halo}/M_\odot) < 11.5$, where HESTIA stellar masses are greater than NIHAO's and greater

than those predicted by abundance matching relations by 1-2 dex. The most massive halos in HESTIA LG simulations are in better agreement with stellar mass - halo mass relations from the literature. The reason for this excess of stars is probably a lack of feedback at masses lower than that of the MW which should be adjusted so that simulated halos follow the abundance matching relations. Also, this is a possible cause for our inability to distinguish tracks of stars from accreted galaxies in HESTIA panels of figure 7: accreted galaxies of lower masses than the MW candidate have an excess of stars that increase the metallicity of the accreted galaxy through nuclear reactions, so the [Fe/H] values of its stars are similar to those of the MW candidate's stars, and they occupy the same region of the [Fe/H] versus age plane. Unlike HESTIA, NIHAO LG simulations follow the stellar mass - halo mass relation, and their dwarf galaxies contain a lower number of stars that are not able to generate as many metals as those of HESTIA. Thus, the [Fe/H] of stars is lower in accreted galaxies than in the MW candidate, which separates both tracks in the [Fe/H] versus age diagram.

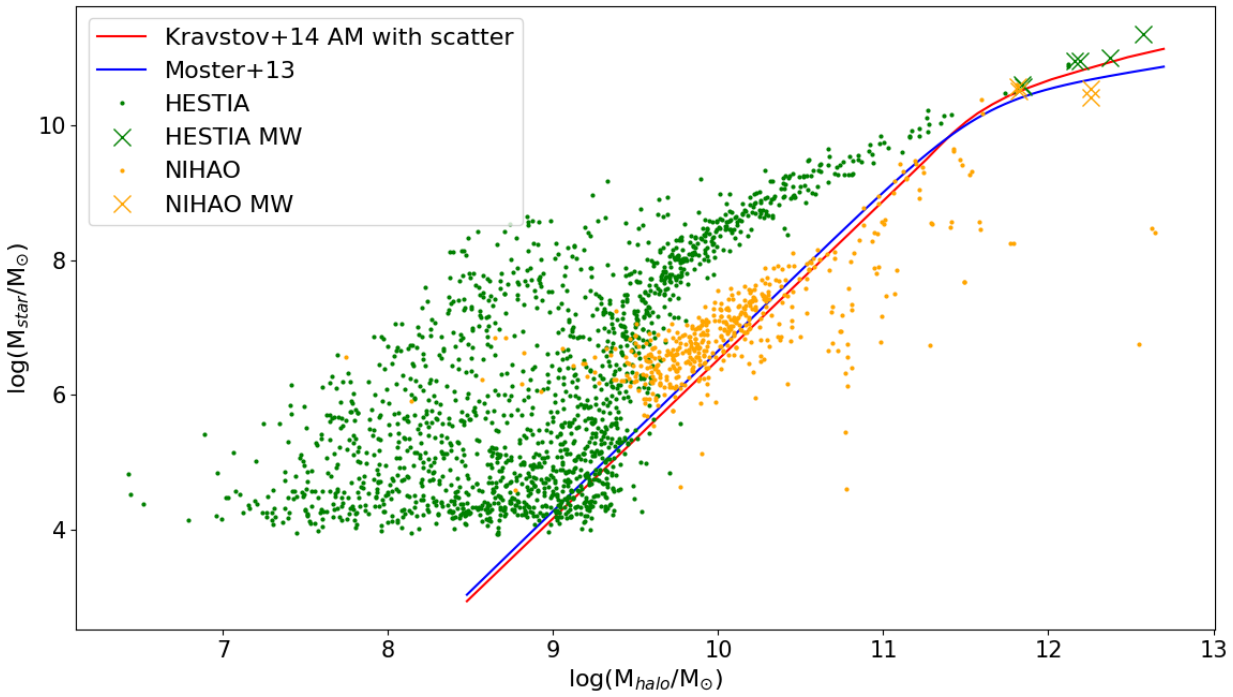

Figure 8: Stellar mass versus halo mass. Dots mark dwarf galaxies in LG simulations. Crosses mark the initial MW candidates in the same simulations. Moster et al. [2012]'s abundance matching relation is plotted as a blue solid line. Kravtsov et al. [2018]'s abundance matching relation with scatter is represented by the red solid line.

5.2. [O/Fe] versus [Fe/H] plane

In figure 9 we plot point density diagrams of solar neighborhood stars of every MW-like galaxy in the [O/Fe] versus [Fe/H]. There are several differences to be pointed out between these panels and the observational data shown in figure 6. We first focus on the general shape of the track of stars in the plane. Most galaxies do show an elbow where the slope of the [O/Fe]-[Fe/H] relation changes. The galaxy nmdh2 is an expected exception, since it can not reproduce the chemical distribution of the MW due to the lack of implementation of metal mixing. The galaxies

g8.28e11 and g7.44e11 present chemical distributions with almost constant [O/Fe] values when compared to the rest, and they do not show a change in the general slope of the [O/Fe]-[Fe/H] relation at any point. These galaxies also showed anomalies in the [Fe/H] versus age diagram in figure 7, with very high recent star formation. This peak of stars correspond to the highest [Fe/H] values in the diagram, so they are located in the rightmost part of the [O/Fe] versus [Fe/H] panels, where we also see an increase in [O/Fe] values. These facts are related to each other because star formation leads to the early death of massive stars in type II supernovae. This process enriches the ISM with α particles such as oxygen. Therefore, very recent high peaks in star formation cause the metal distribution of the simulated galaxy to deviate from the observed one in the MW. We do not notice this effect in the same way for simulation 09_18h2, which also presents recent star formation. Snaith et al. [2015] state that most stars in the MW disk were formed during the first 4-5 Gyr of its evolution, and that star formation has remained low and constant for the rest of the MW life. According to that, galaxies g8.28e11, g7.44e11 and 09_18h2 are not good MW study cases.

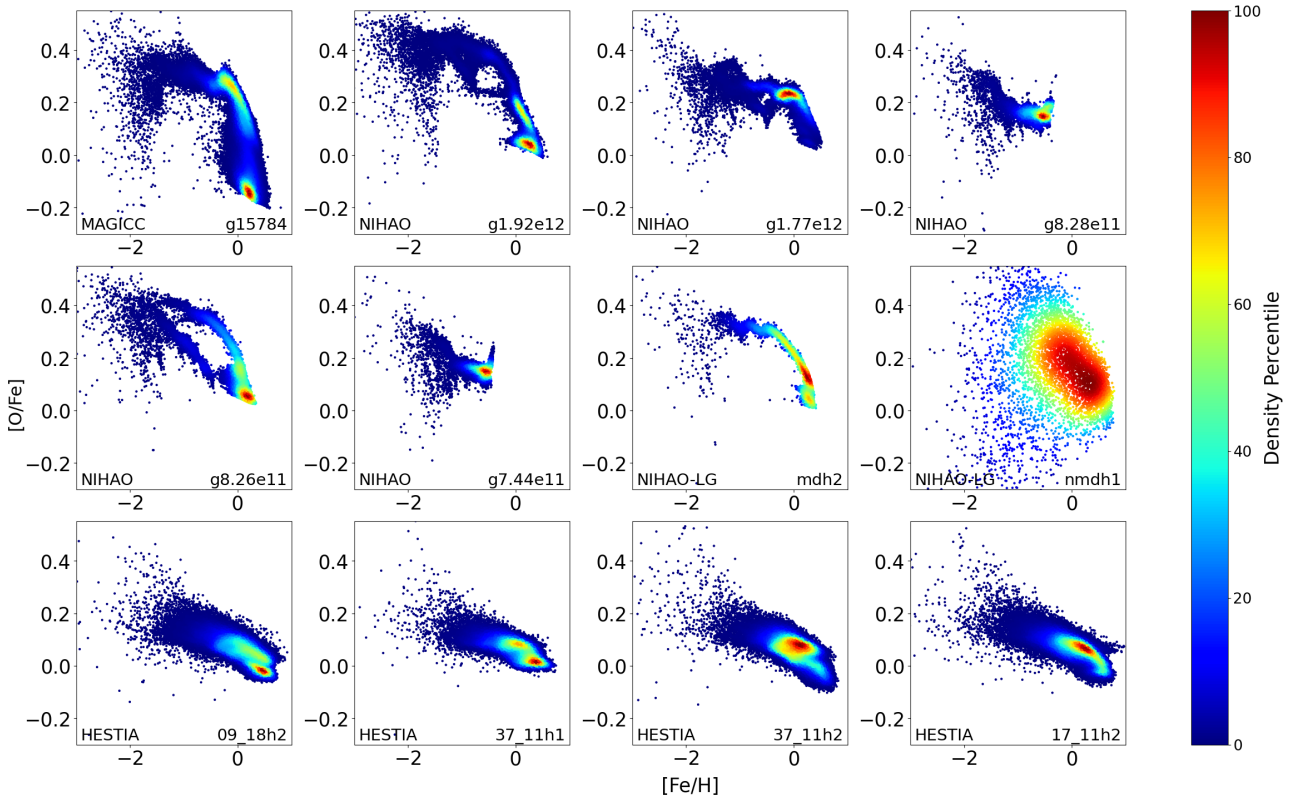

Figure 9: [O/Fe] versus [Fe/H] point density diagram of the stars in the solar neighborhood of the selected simulated galaxies.

5.3. Metal distribution in the solar neighborhood

We have stressed during all the work which are the differences between the ways in that each simulation deal with metal diffusion. We also noticed contrasting chemical distributions of simulations with different metal diffusion implementations (see figures 7 and 9), and we want to further study their effects on the results of simulations. In this section we study three representative galaxies with different metal diffusion in order to determine which of them leads to the results most similar to MW observations from GALAH DR3 (since we are carrying

out this comparison, we use the solar neighborhood selection described in section 4.3 during this current section), and hopefully constrain the necessary strength of metal diffusion in simulations for matching MW observations. The chosen galaxies are, from strongest to weakest metal diffusion: NIHAO-LG's SPH simulation with Wadsley et al. [2008]'s sub-grid diffusion model (mimicking Eulerian diffusion's strength), HESTIA's quasi-Lagrangian simulations and NIHAO-LG's simulation suite with no metal diffusion. There are 4 HESTIA galaxies among the MW candidates we selected. We choose one from them for this comparison, based on their similitude to NIHAO simulated galaxies. In figure 7 we see that galaxies 37_11h1, 37_11h2 and 17_11h2 show star formation peaks at similar times to NIHAO simulations. The galaxy 09_18h2 has a very recent peak of star formation so we discard it for this purpose. Then, the total mass of 17_11h2 is much more comparable to those of NIHAO simulated galaxies than 37_11h1 and 37_11h2. We therefore choose 17_11h2 as a example case of HESTIA simulations to compare with NIHAO md and NIHAO nmd.

Figures 10 and 11 show the histograms of [Fe/H] for stars and gas particles respectively selected in the solar neighborhood of the simulation.

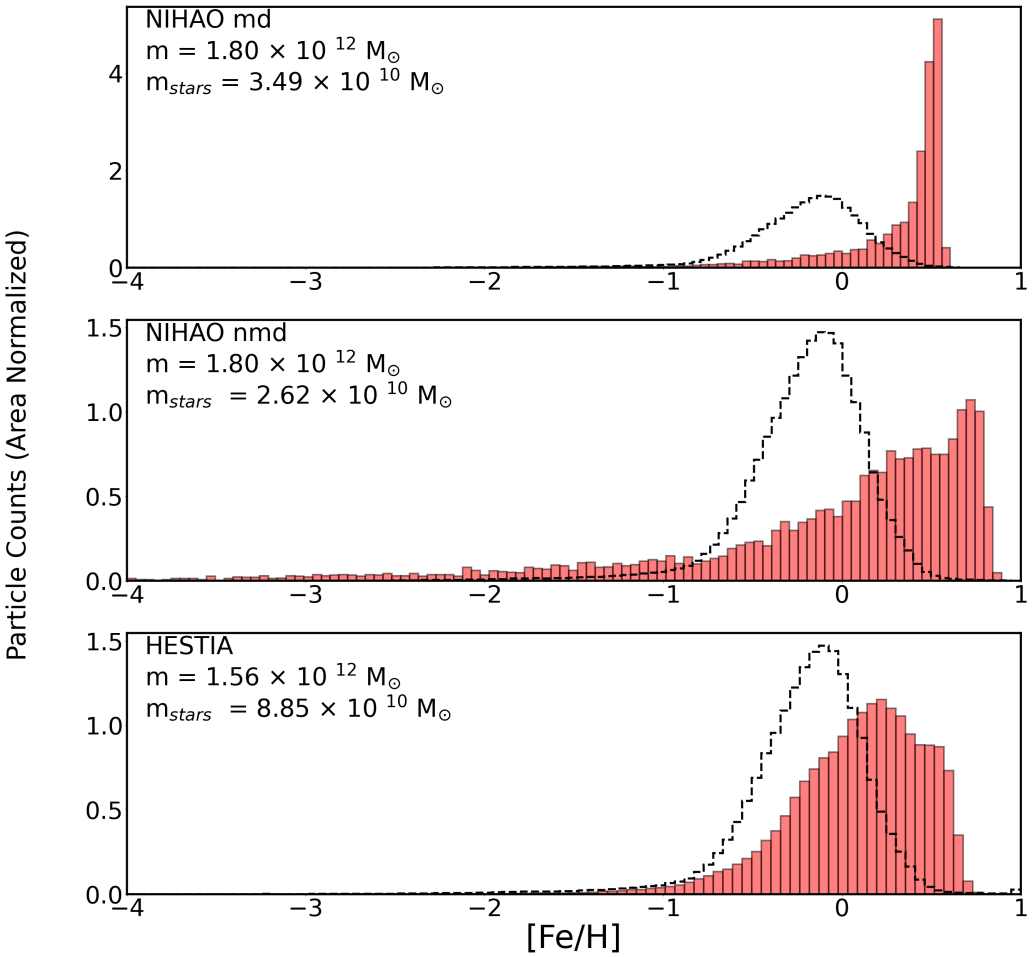

Figure 10: [Fe/H] histrogram of stars in the solar neighborhood. The areas of histograms are normalized to unity. GALAH DR3 data is shown as black dashed lines. From top to bottom: NIHAO-LG md most massive halo, NIHAO-LG nmd most massive halo, HESTIA's 17_11h2.

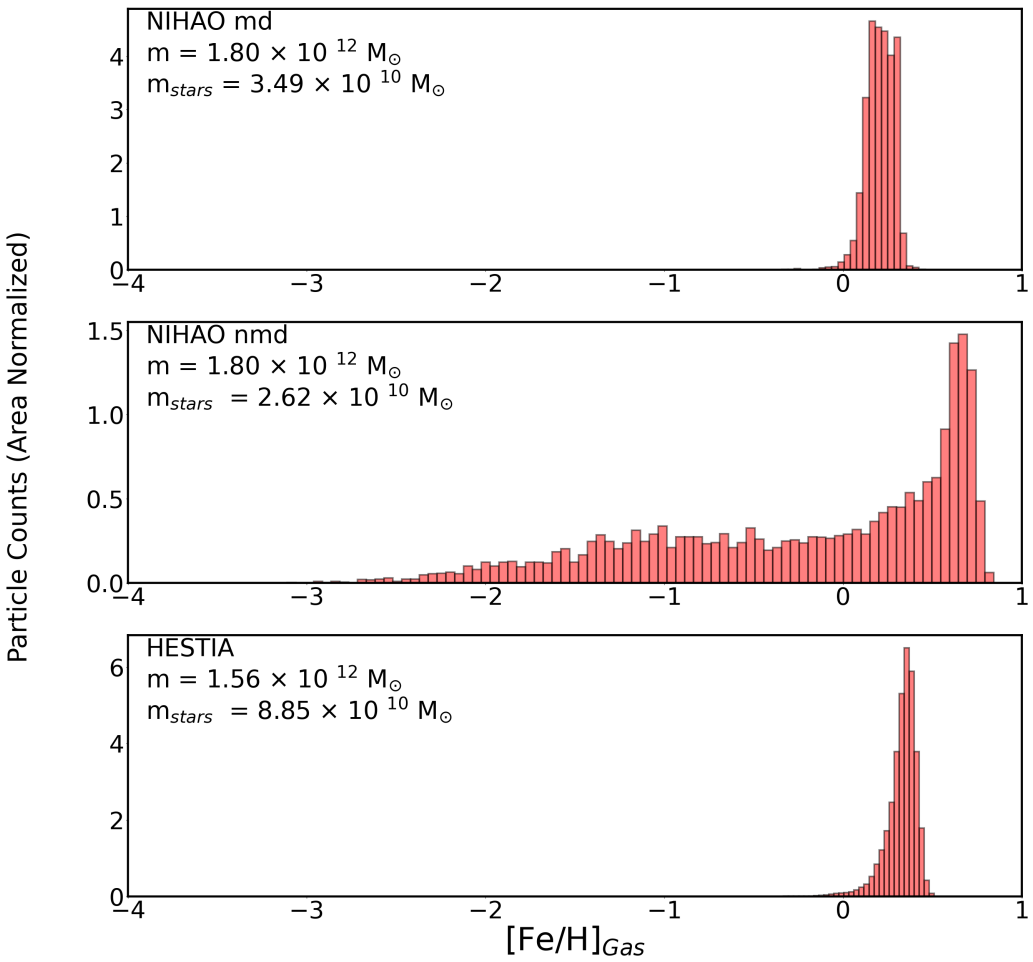

Figure 11: [Fe/H] histrogram of gas in the solar neighborhood. The areas of histograms are normalized to unity. From top to bottom: NIHAO-LG md most massive halo, NIHAO-LG nmd most massive halo, HESTIA's 17_11h2.

In figure 10 we can see how every simulation has overall more metallic stars than GALAH DR3 data in their solar neighborhood region. This is especially noticeable in both NIHAO histograms over that of HESTIA, whose distribution peak is closest to that of observations. In all cases, the simulations' distribution is more skewed towards higher [Fe/H] values than that of the observed stars, presenting too many stars with metallicities lower than the peak of the distribution and too few with higher metallicities than the peak. The latter is again less noticeable for HESTIA's 17_11h2 galaxy. We see large variations in the [Fe/H] spread from one simulation to another. As expected, NIHAO nmd's [Fe/H] spans over a wide range of values (~4 dex) due to its lack of metal diffusion. In comparison, NIHAO md's data is much more concentrated, ranging over roughly 1.5 dex and having a very clear peak close to 0.5. The addition of metal diffusion highly changes the resulting [Fe/H] distribution, homogenizing the metallicity values of stars. HESTIA data serves as an intermediate case between the two previous ones, since the metallcity of stars in its solar neighborhood spans over ~3 dex. This is again consistent with the theoretical strength of metal diffusion of quasi-Lagrangian methods. HESTIA's [Fe/H] dispersion is the most similar to that of GALAH DR3 observations. NIHAO's nmd distribution is too spread to reproduce GALAH DR3 data, implying that some metal dispersion is needed in order to simulate the actual metal mixing in MW's formation. However NIHAO's md metal diffusion is too strong compared both to HESTIA's quasi-Lagrangian treatment and to GALAH DR3 observations. In fact, it seems that

NIHAO md's metal diffusion is so excessively strong that this simulation shows less agreement with observations than NIHAO nmd.

As depicted in figure 11, we find that gas [Fe/H] distributions are less disperse than those of stars, and their peaks are more pronounced, except in the case of NIHAO md, whose star [Fe/H] distribution is extremely peaky.

Figure 12 gives a more general vision of the distribution of metals in the solar neighborhood stars by showing the [O/Fe] versus [Fe/H] phase space. In this representation we can see additional details of the distribution, such as the two separated maxima in NIHAO md distribution. These maxima have very similar [Fe/H] values, which result in the strong peak seen previously in figure 10. We observe that the simulations' maxima are located at too high [Fe/H] and [O/Fe] compared to GALAH DR3 data, whose maxima is located at solar values as expected of the solar neighborhood. However, HESTIA's simulation distribution is notably better centered than the rest in the [O/Fe] dimension. The slopes of the distributions are visually similar for both NIHAO simulations. HESTIA's data deviates from this trend, presenting an attenuation in the slope compared both to NIHAO simulations and GALAH observations. NIHAO md distribution reproduces correctly the spread of observations in the direction of the slope, but it is too narrow in the direction perpendicular to the slope. NIHAO nmd spreads excessively in both directions. HESTIA's data approximates best the spread of observations in [Fe/H] as we deduced from figure 10, despite the off-center location of the distribution in the [O/Fe] versus [Fe/H] plane.

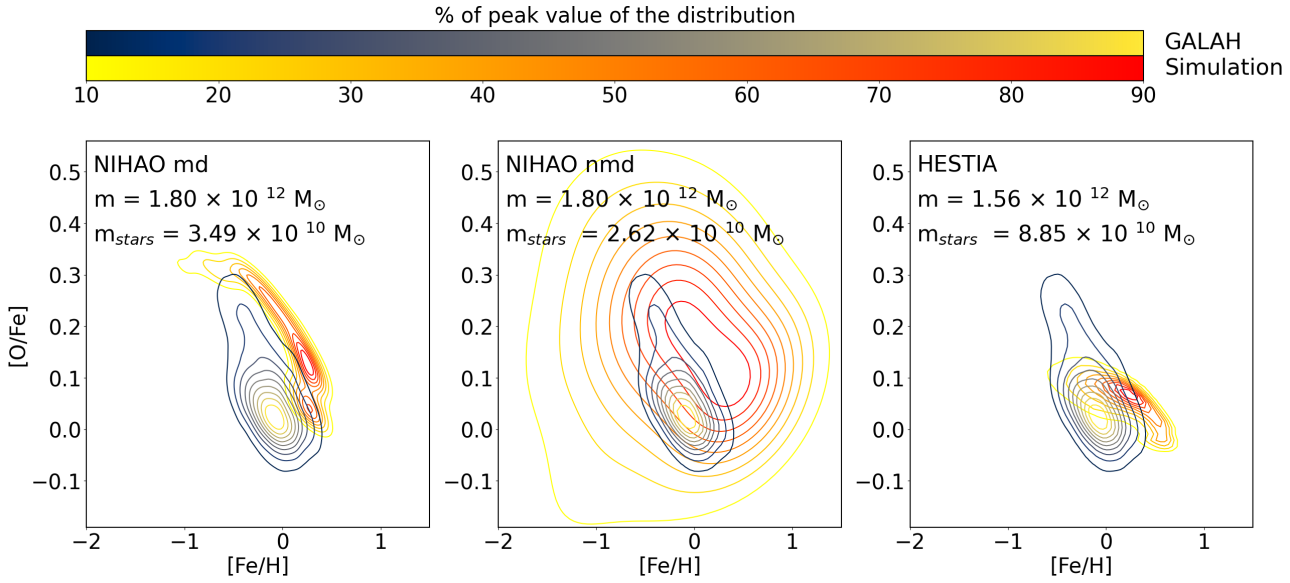

Figure 12: [O/Fe] versus [Fe/H] plane. The yellow to red lines represent data from simulations and the blue to yellow lines represent GALAH DR3 data. Contours are drawn at 10%-90% of the peak of the distributions. From left to right: NIHAO-LG md most massive halo, NIHAO-LG nmd most massive halo, HESTIA's 17_11h2.

In order to quantify the spread of simulations' distributions compared to that of observations in the [O/Fe] versus [Fe/H] phase space, we calculate the areas enclosed by contours in figure 12. We calculate the deviation of the area (a1) for the contour at a percentage x of the peak of the distribution of each simulation with respect to the area (a2) of the contour at the same percentage of the peak of the observed distribution (Deviation (%) = (a1/a2 - 1) × 100). In table 2 we present the values of the deviations of areas enclosed by contours at 10 - 90 % of the peak value of the distributions. NIHAO's simulation with no metal diffusion exhibits much more

dispersion than observations in the [O/Fe] versus [Fe/H] space according to this indicator, with deviations of around 1000%. HESTIA 17_11h2 and NIHAO mdh1 present underscatter with respect to GALAH data, both with deviations of the order of -50%. The deviations remain almost constant at all contour levels of the HESTIA simulation, whilst NIHAO mdh1 reaches more similitude with the scatter of observations at the outermost contours. The results of this analysis contrast with those of the one-dimensional distribution of [Fe/H] we previously performed. In the former study, we observed better agreement of HESTIA simulations with observations, but when including the [O/Fe] distribution, NIHAO mdh1 seems to overperform HESTIA when reproducing the observed scatter of chemical elements in the MW.

Table 2: Enclosed area deviations from observations for contours at different percentages of the peak value of the [O/Fe] versus [Fe/H] 2d histograms of the solar neighborhood of simulated galaxies.

% of peak	Deviation (%)		
value	md	nmd	HESTIA
10	-54.4	1630	-69.2
20	-52.5	1450	-60.4
30	-49.4	1310	-56.6
40	-24.4	1190	-54.7
50	-10.8	1090	-48.4
60	-9.8	1010	-40.8
70	-14.9	929	-37.8
80	-26.3	758	-43.8
90	-37.2	657	-49.6

Furthermore, we aim to compare the simulations to LOS observations made by De Cia et al. [2021] in the solar neighborhood region. They observe stars between ~0.1 kpc and 3 kpc away from the Sun in order to determine the metallicity of the ISM gas in the line of sight. We show their measurements in figure 13. In order to make similar estimations from simulations data, we select gas particles in cylindrical volumes, one of whose basis is centered in a potential Sun location. We select 20 potential Sun locations in the galactic plane and equally separated in the polar direction at 8 kpc from the galactic center. From each of these locations, we make 30 cylindrical volume selections, again centered in the galactic plane and equally separated in the polar direction. Cylinders range from 0.5 kpc through 2.5 kpc with an uniform distribution. The lower limit is set to 0.5 kpc in order to make it less probable to not get any particle inside the volume, and the upper limit is set to 2.5 kpc rather than 3 kpc because it better represents most part of De Cia et al. [2021] observations. The radius of the cylinders is set to 0.05 kpc because the softening length of our simulations in the solar neighborhood region is in the order of 0.1 kpc, so this value of the radius is appropriate for making cylinders as thin as possible (trying to reproduce LOS observations) but ensuring that not too many selected volumes are empty of gas particles.

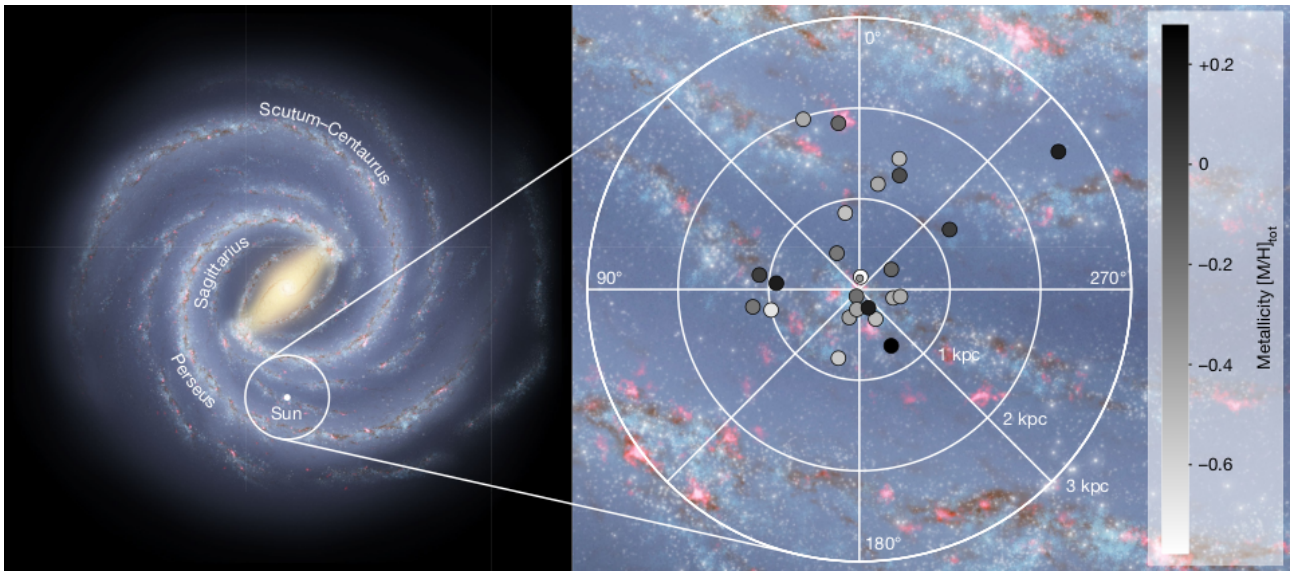

Figure 13: Source: De Cia et al. [2021]. Left: artistic impression of the Galaxy, face on. Image courtesy of NASA/JPL-Caltech/R. Hurt (SSC/Caltech). Right: the location of De Cia et al. [2021]'s observation targets is marked on the same illustration of the galaxy, but zoomed-in on the star-forming spiral arms in the solar neighborhood. The metallicity of the neutral gas along these lines of sight is highlighted with the gray scale.

Figure 14 shows the selected potential Sun locations over a line of sight averaged density face on image of the gas in the galaxies. It also contains zoom-ins centered in specific potential Sun locations, where we can see the averaged values of the particles in each cylindrical volume, represented as circles located at the end of the cylindrical volume. These circles are plotted over a face on image of the [Fe/H] distribution of gas averaged over the zenithal line of sight (of the face on projection) over a slice of 2 kpc over and under the galactic plane (the slice has a total depth of 4 kpc). The pixel size is 0.1 kpc matching the order of magnitude of the softening length. The colorbars are centered in the median of LOS "observations" and range over 1.1 dex, imitating the [Fe/H] range shown in De Cia et al. [2021] figure 1. This representation allows for easy interpretation and comparison of the metallicity distribution of gas in simulations and in observations.

We observe that the results of LOS simulated observations in NIHAO mdh2 are highly uniform and similar to the median value. Instead, NIHAO nmdh1's gas has much more disperse [Fe/H] values, as represented by the variations in the color of the plotted circles. This stresses that NIHAO nmd has more similar [Fe/H] dispersion to that of De Cia et al. [2021] observations than NIHAO md. As per usual in this analysis, HESTIA's 17_11h2 lies in a midpoint between NIHAO md and nmd. LOS results of these simulations show more metal dispersion than NIHAO md and less than NIHAO nmd. It is not straight forward to tell if NIHAO nmd fits De Cia et al. [2021] observations better than 17_11h2 from this figure alone. 17_11h2's results show less [Fe/H] dispersion than De Cia et al. [2021] observations, specially lacking of gas at the lowest [Fe/H] end. However, NIHAO nmd's dispersion may be (and it probably is) too high, since the darkest circles in the mid panel of the right column are likely to represent [Fe/H] values out of the range of the colorbar.

We must also take into consideration Esteban et al. [2022]'s results, which point towards a highly uniform metal distribution of the solar neighborhood. If that was the case, then NIHAO md would be the simulation in most agreement with the actual distribution of the solar

neighborhood. HESTIA 17_11h2's results could also be conciliated with Esteban et al. [2022]'s as we discuss in the next paragraph.

ç

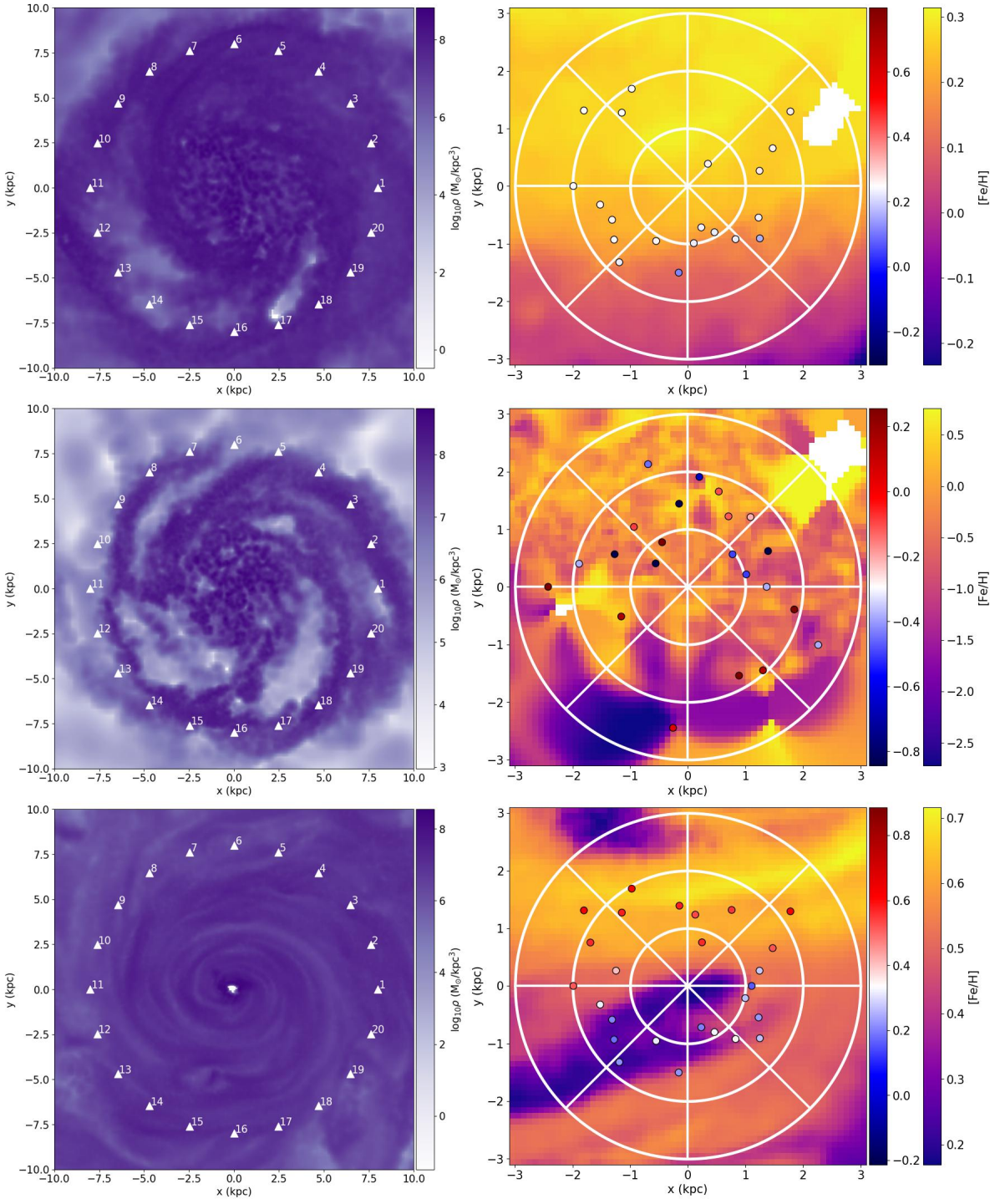

Figure 14: Left: Face on LOS averaged mass density map of gas in the simulated galaxy. The potential Sun locations we studied are marked with white triangles and labelled. Right: Zoom-in of potential Sun location 16. The background shows an averaged [Fe/H] map of a slice of width 0.5 kpc centered on the galactic plane. The pixel size is 0.1 kpc. White rings mark radial distances of 0.5 kpc, 1.5 kpc and 2.5 kpc from potential Sun location 16. Pixel size is 0.1 kpc. Colorbars for LOS points are centered in the median value of LOS "observations" and their range is set to 1.1 metallicity dex. From uppermost to lowermost panel: NIHAO md, NIHAO nmd, HESTIA 17_11h2.

The same comparison for other potential Sun positions is shown in the appendix 6. In all of these we keep observing the extreme colors of the blue-red colorbar in NIHAO nmd's panels. This is in agreement with our interpretation of NIHAO nmd's [Fe/H] values being too disperse compared with De Cia et al. [2021]'s observations. We find several positions where the dispersion of [Fe/H] values is similar for NIHAO md and 17_11h2 (e.g.: figures A.1, A.2, A.3 among others). The similitude between NIHAO md and 17_11h2 at some Sun locations may indicate that 17_11h2's gas [Fe/H] is too mixed compared with the actual MW, according to De Cia et al. [2021], or that it has a fairly correct amount of mixing, according to Esteban et al. [2022]. In other cases we find a similar situation to what we observed for potential Sun location 16 of 17_11h2' in figure 14 (e.g.: figures A.5, A.8, A.18).

5.4. Low metallicity stars

A clear advantage of using simulations for studying the formation of galaxies is that we can access all the intermediate states of a simulation over the evolution of the system. We make use of this possibility for tracking specific stars over the full time of the simulation. All particles in the simulation have individual ID numbers that we use for this purpose. Since star particles are formed at a specific time from former gas particles, we need to track them too. This is also possible because every star particle stores the ID of its parent gas particle.

In order to select stars of interest, we use [Fe/H] versus age diagrams. These are shown for the selected galaxies in figure 7. We are interested in low metallicity outliers in the [Fe/H] versus age diagrams due to Sestito et al. [2020b]'s findings of UMP stars in the MW disk. The presence of so many such stars in the solar neighborhood is only expected if the region presents notable variations in metallicity, as claimed by De Cia et al. [2021] and contradicting Esteban et al. [2022]. NIHAO's nmdh1 represents that situation. On the other hand, when we have a homogeneous ISM, we seem to get almost no low metallicity disk stars, suggesting that diffusion rates are too high, as also indicated in Table 2 for both NIHAO with no metal diffusion and HESTIA. After identifying these stars in a simulation, we try to unveil where they came from and to justify their deviation from the bulk of stars in metalliciy and/or age. We find several of these stars in galaxy g15784 and we select 18 of them (see left panel in figure 15), which are clearly divided in two groups: a group of young stars with lower [Fe/H] values than the bulk of stars, and a group of older stars with even lower [Fe/H] values. The rest of the selected MW candidates do not contain as many outliers that we consider worth tracing back, with the exception of nmdh1, and we skip this analysis in them for the sake of time. Another reason to prioritize the study of g154784 over other simulated galaxies is that this simulation has been widely researched and it is considered to be one of the best at reproducing traits of the actual MW (e.g.: Miranda et al. [2016], Gallart et al. [2019], Brook et al. [2020]).

After selecting the stars of interest by setting limits in the age and metallicity diagram, we track their formation and evolution. We make side on renders of each snapshot adjusting the limits of the image so that all tracked stars are contained in it. The presence of background side on images of the galaxy is useful since it also allows us to see when the stars enter the disk of the galaxy. We label each star and plot them over the rendered image in green if they are still gas particles or in red if the star is already formed. We classify the stars in three groups

according to their provenance: "star accreted", if the star formed before entering the main halo; "gas accreted", if the star was still in gas form when it entered the main halo from a different one; and "in situ", if the gas that formed the star was accreted directly from the intergalactic medium (IGM) into the main halo without previously belonging to a different halo. We store the properties of the stars at the time of the first snapshot when they were already formed, as estimations of their properties at the real formation time. We know their actual formation time by their age, but we can not recover their properties at the exact formation time since snapshot times do not necessarily coincide with formation times. We also estimate the time they entered the main halo as the time of the first snapshot where the stars are bound to it. We construct the Toomre diagram of the solar neighborhood stars at z = 0 and overplot the tracked stars to check if they are kinematically a part of the disk or not. The Toomre diagram shows the velocity space, with the polar component in the Y-axis and the quadratic sum of vertical and radial velocities $\left(\sqrt{V_R^2 + V_Z^2}\right)$. This representation is commonly used for discerning the major kinematic components of the galaxy, namely the disk (thin and thick) and the halo (e.g. Venn et al. [2004]).

We show the stars we selected from g15784's solar neighborhood by marking them on the [Fe/H] versus age diagram in the left panel of figure 15.

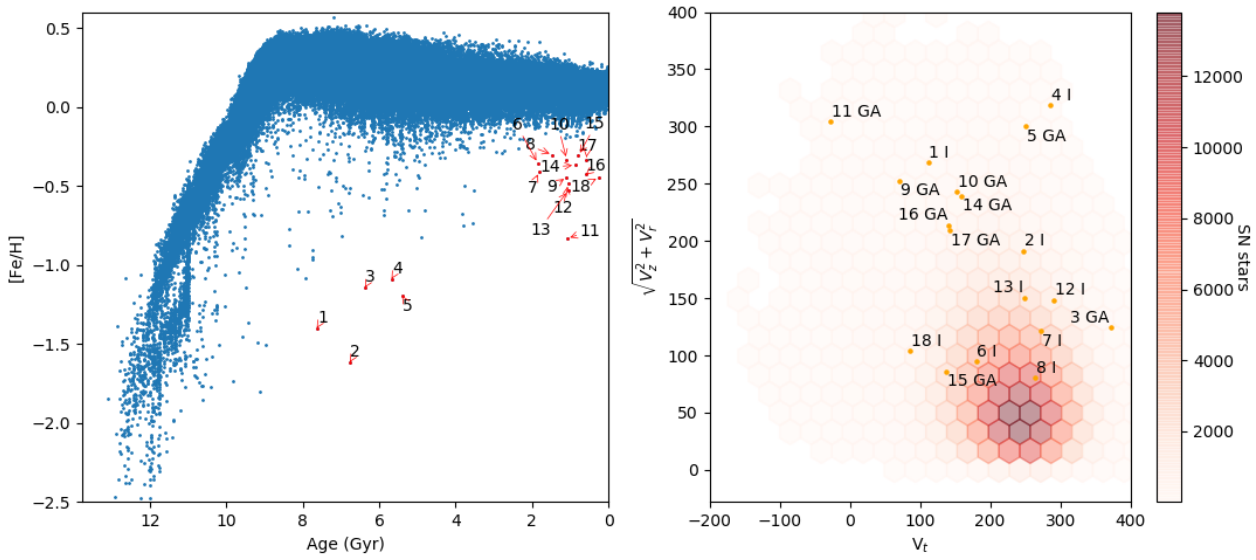

Figure 15: Left: [Fe/H] versus age diagram of stars in the solar neighborhood of galaxy g15784. Tracked stars are marked in red. Right: Toomre diagram of stars in the solar neighborhood (SN) of galaxy g15784. Stars are labeled according to their age starting from the oldest one. In the Toomre diagram the labels include the accretion classification.

Since these stars are selected from the solar neighborhood, they are spatially in the disk of the galaxy in the last snapshot at redshift z = 0. However, they may not correspond to the disk kinematically. For testing this, we plot the Toomre diagram (right panel of figure 15) of all solar neighborhood stars as a 2-D histogram, and we plot the selected stars over it. We assume the solar neighborhood represents the disk in the Toomre diagram, as most stars spatially located in the disk are expected to have disk-like kinematics. We confirm this looking at the Toomre diagram: solar neighborhood stars occupy a region of high polar velocity components compared to radial and vertical components. Therefore if a star lies close to the bulk of stars in

this diagram, we identify it as a disk star, whilst we consider than the rest of stars pertain to the halo component. We flag tracked stars according to the flags described in the beginning of this section. We find no stars in the category "star accreted", 9 "in situ" stars and 9 "gas accreted" stars. Thus, all the stars we tracked entered the MW-like galaxy in gas form, either from the merger of another galaxy into the main one or directly from the IGM.

In the Toomre diagram we notice that all "in situ" stars except two of them (1I and 4I) are located close to most solar neighborhood stars. Similarly, all "gas accreted" stars except two of them (3GA and 15GA) lie far from solar neighborhood stars. According to our previous assumption, we identify all "in situ" stars except 1I and 4I as disk stars, and all "gas accreted" stars except 3GA and 15GA as halo stars. A plausible explanation for this general trend is that "in situ" stars adapt more easily to the kinematics of the disk because their gas particles enter the MW individually or in small groups from the IGM, with little previous velocity components that are modified by the interaction with the rest of particles in the galaxy, which move preferentially rotating in the disk plane around the center of the galaxy. "Gas accreted" particles, conversely to "in situ" particles, generally enter the MW in large groups in merger processes. These phenomena are complicated and chaotic interactions between all stars, gas and dark matter of both galaxies, and the resulting trajectory of a specific gas particle is less predictable. The interaction between two large groups of particles with radically different general motions makes it more likely for accreted particles to adopt dispersion-dominated trajectories rather than rotation-dominated trajectories, thus justifying their binding to the halo component of the MW. This hypothesis should be further testes by studying the properties of the individual galaxies accreted during the simulation. The interpretation problem, aside from pure stochasticity, remains for the specific stars that do not follow the general trend explained for their category. We further study them by gathering their times of accretion into the MW (T1) and their formation times (T2) in table 3. We plot the difference between those two times for every tracked star.

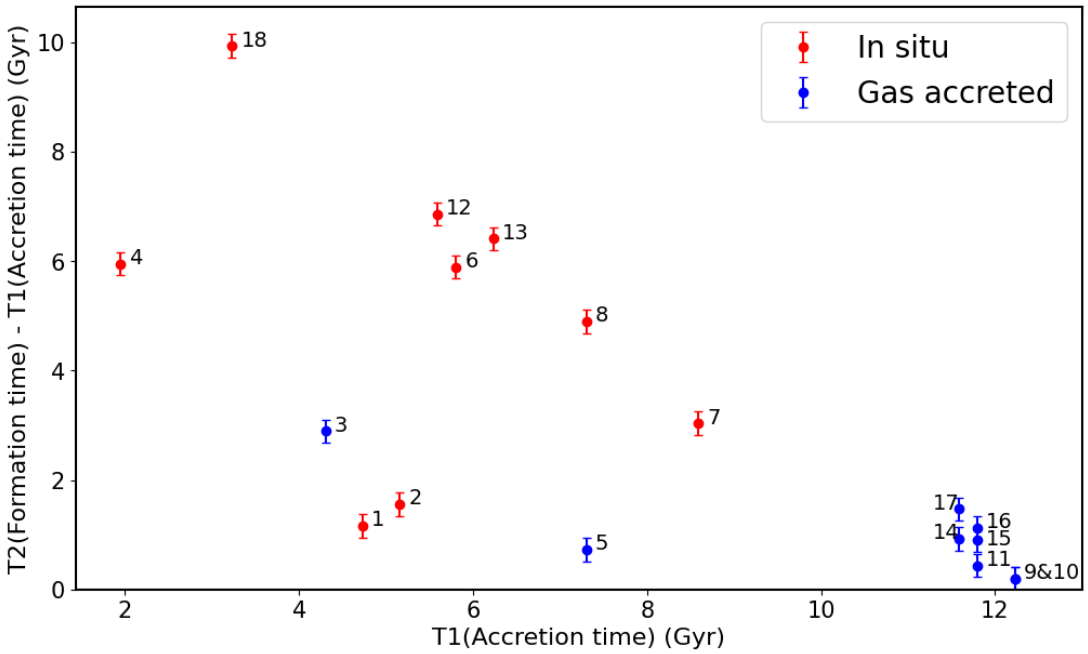

Figure 16: Time elapsed since the approximated instant a tracked particle entered the main halo of g15784's simulation until the time it formed a star. Particles are marked in the figure by their label.

Figure 16 shows graphically that the uncertainty over the accretion times of stars 9 and 10 is higher than the time elapsed between their accretion and formation, which is also shown in table 3. This means that there is a possibility for them to fall into the ”star accreted” category. We also notice a general trends for ”in situ” stars to spend more time in the main halo in their gas form than ”gas accreted” particles do. This is presumably caused by the violent nature of merger processes where ”gas accreted” particles enter the MW, since they are likely to trigger star formation. This may be related to the trend noticed in figure 15: the dynamics of gas particles are more easily modified by and adapted to their environment than those of star particles, as gas cools down and falls into the disk whilst stars preserve their temperature. Thus, gas particles are more likely to end up following the general motion of the disk than to have disperse trajectories. This is probably also the explanation to the absence of ”star accreted” particles among the selection: particles that enter the halo in star form will maintain their temperature and they are unlikely to fall into the disk region where we selected particles for tracking. We note that star 1, which deviates from the general trend of ”in situ” stars in the Toomre diagram, is also the ”in situ” star with the lowest T2-T1 value. Similarly, star 3 deviates from the general trend of ”gas accreted” stars in the Toomre diagram, and it is the ”gas accreted” star with the largest T2-T1 value. This fact is a candidate for explaining why they do not follow the behavior of other stars in their same category, if we follow our previous reasoning relating higher T2-T1 values with the likelihood of a star ending up having disk-like kinematics. However, the kinematics of stars 4 and 15 can not be explained in the same way. We note that most ”gas accreted” stars were accreted very recently into the main galaxy, and they probably share their origin in the same accreted galaxy. Studying this specific merger could be of help for understanding the resulting kinematics of ”gas accreted” stars.

Table 3: Time of accretion into the main halo (T1) and formation time (T2) of tracked stars, together with time passed between T1 and T2. The beginning of the simulation is considered as time value 0. T1 is determined by the time of the first snapshot where the particle is bound to the main halo, so there is a margin of error equal to the time passed between snapshots (0.21 Gyr).

Star label	T1 (±0.21Gyr)	T2 (Gyr)	T2-T1 (±0.21Gyr)
1	4.73	5.89	1.16
2	5.16	6.71	1.55
3	4.30	7.20	2.89
4	1.95	7.90	5.96
5	7.30	8.03	0.72
6	5.80	11.70	5.90
7	8.59	11.62	3.03
8	7.30	12.21	4.90
9	12.23	12.42	0.19
10	12.23	12.43	0.20
11	11.80	12.24	0.44
12	5.59	12.45	6.87
13	6.23	12.65	6.41
14	11.59	12.51	0.92
15	11.80	12.71	0.91
16	11.80	12.92	1.12
17	11.59	13.05	1.47
18	3.23	13.17	9.94

We plot the positions of tracked stars over a render of the simulation in the side on projection of the main halo in every snapshot of the simulation. The images are centered on the main halo. We can see this representation in figure 17, which allows us to follow the trajectories of tracked stars during their evolution until they arrive to the MW's disk. In the very first panel (top left) we see the first record we have of the positions of the tracked particles, 1.089 Gyr after the beginning of the simulation. We see how most "gas accreted" particles are concentrated in the right side of the image, close to some luminous matter. This suggests that there is a high concentration of matter in that region, and that they are likely to enter a different halo soon, before making their way into the main one. On the other hand, "in situ" stars are disperse and separated from luminous matter, meaning they lie in less dense regions where there are less nearby halos to enter. Particle 4I is an exception, located right next to the most luminous region of the image. This region, however, is the main halo, so even if this particle enters its neighbor halo at early times, it will be classified as an "in situ" stars. We confirm this with its T1 value in table 3, which is only 1.95 ± 0.21 Gyr. Considering this, it is even more surprising that this star is found to be kinematically a part of the halo at z = 0, since its trajectory should have adapted to the general motion of the MW's disk during the long time the star has inhabited the galaxy.

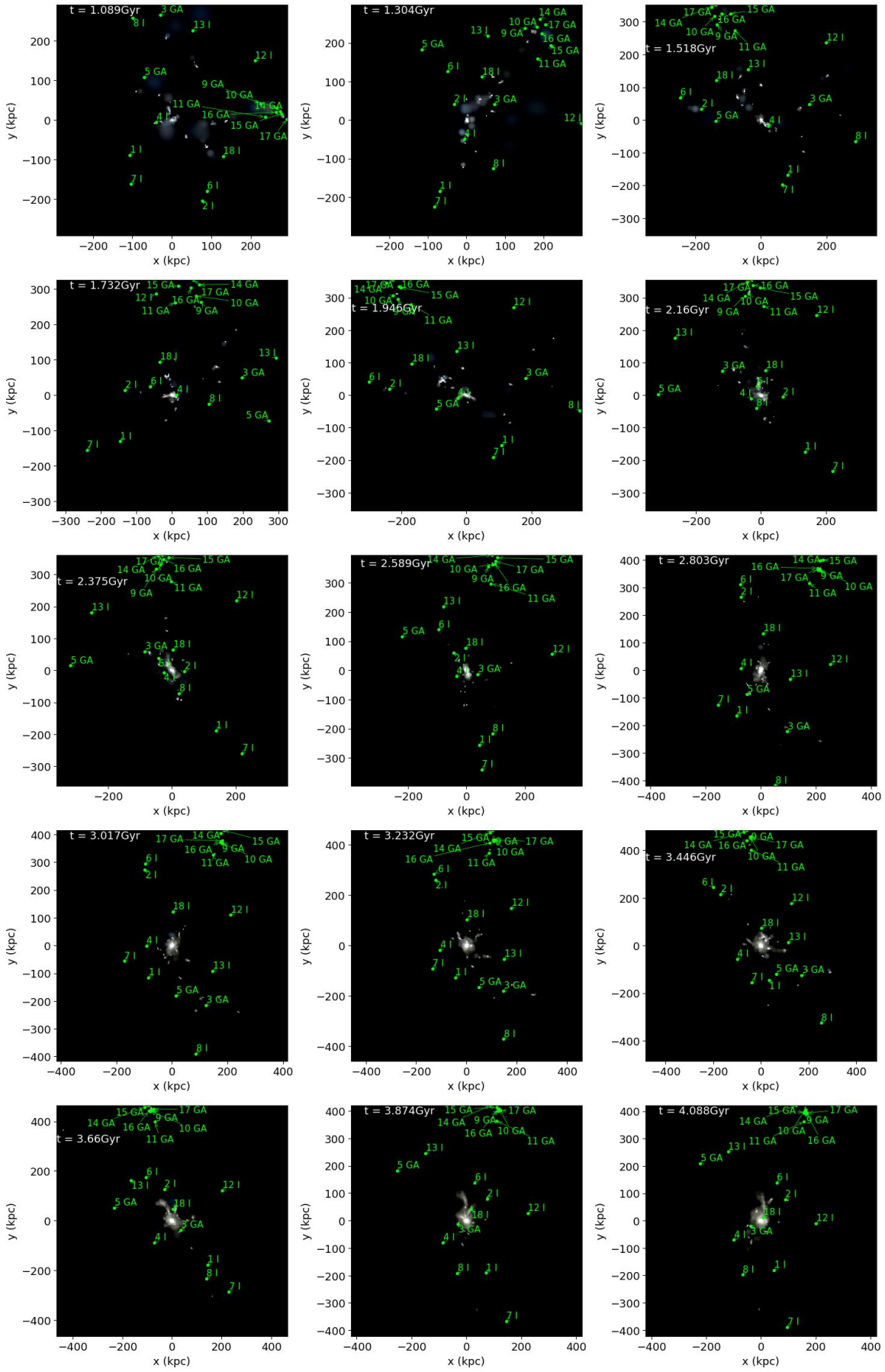

Figure 17: Panels 1 through 15. Side on renders of g15784 for all 59 snapshots available over the evolution of the simulation. Selected star particles are shown either in their gas form (green) or after the star has already formed (red). The limits of the plots are adjusted to tightly contain all selected particles at all panels.

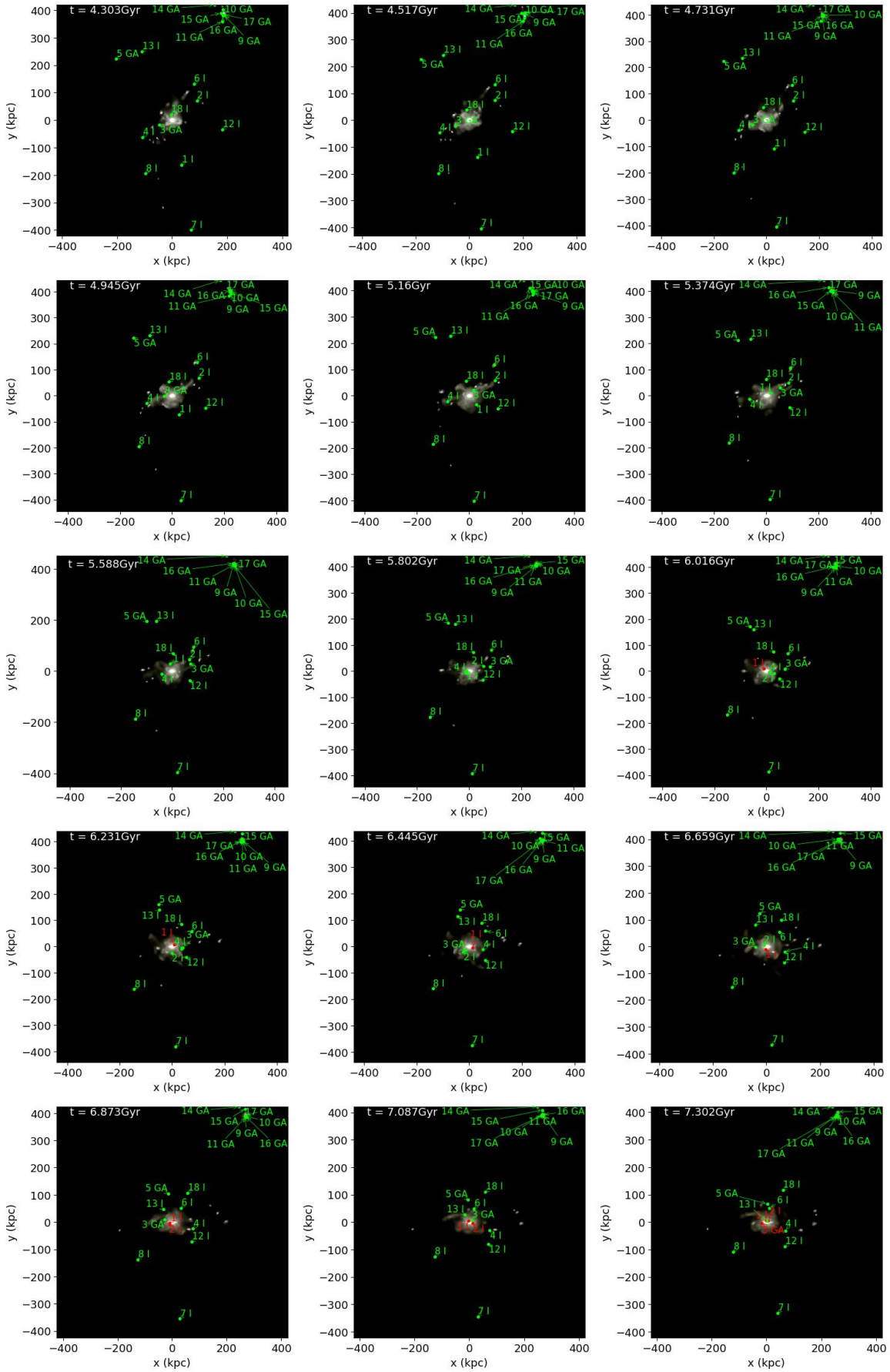

Figure 17: Panels 16 through 30. Side on renders of g15784 for all 59 snapshots available over the evolution of the simulation. Selected star particles are shown either in their gas form (green) or after the star has already formed (red). The limits of the plots are adjusted to tightly contain all selected particles at all panels.

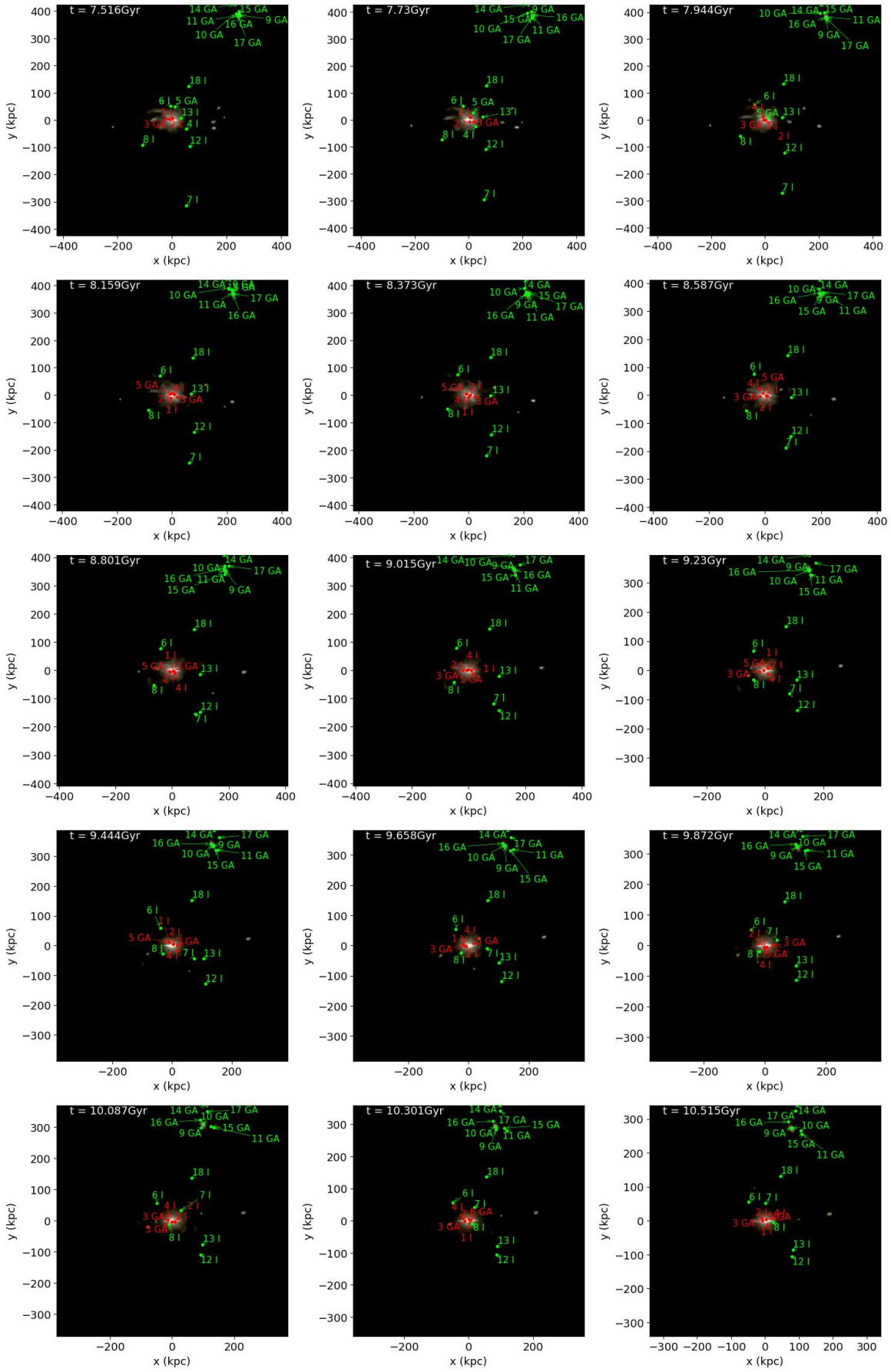

Figure 17: Panels 30 through 45. Side on renders of g15784 for all 59 snapshots available over the evolution of the simulation. Selected star particles are shown either in their gas form (green) or after the star has already formed (red). The limits of the plots are adjusted to tightly contain all selected particles at all panels.

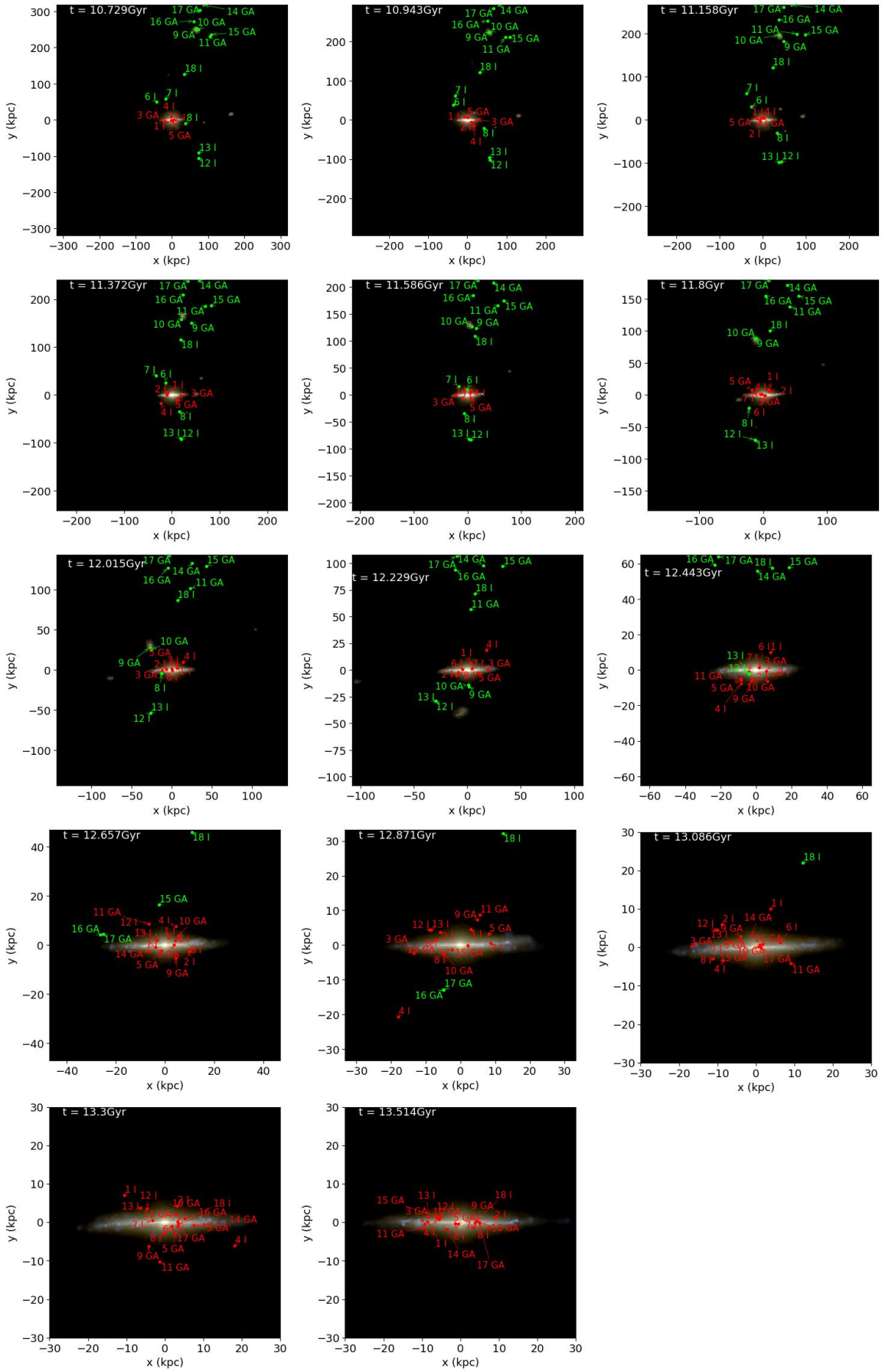

Figure 17: Panels 46 through 59. Side on renders of g15784 for all 59 snapshots available over the evolution of the simulation. Selected star particles are shown either in their gas form (green) or after the star has already formed (red). The limits of the plots are adjusted to tightly contain all selected particles at all panels.

Aside from g15784, the rest of the selected galaxies show few low metallicity outliers in figure 7. However, NIHAO nmdh1 is an exception. The simulation contains a large number of low [Fe/H] stars. The selection process for tracking stars from nmdh1 is different from that performed in g15784. This is because in this case we can not identify isolated groups of stars in the [Fe/H] versus age diagram. We decide to select a group of the youngest, least metallic stars by imposing hard limits at 2 Gyr of age and [Fe/H] value of -1.5. This results in the selection of 215 stars. This quantity of selected stars calls more for a statistical analysis than for the labeling and tracking of each individual star. The selection is showed 18, just like for g15784 but without labeling due to the abundance of stars in the diagrams. We perform the tracking process and label the selected stars with the same flags listed before in this section. We do not show the trajectories of tracked stars with respect to side on renders of the main halo because of the large number of selected stars. We find 98 "in situ" stars and 117 "gas accreted" stars. Once again, no "star accreted" stars are found among the selected stars. This reinforces our previous argumentation about particles that enter the galaxy in their star form being unable to fall into the disk because they can not cool down. An unexpected outcome of this new tracking process is the finding of all selected stars being kinematically a part of the disk (see right panel of figure 18) regardless of their "in situ" or "gas accreted" flag. This differs from what we observed in figure 15 for galaxy g15784.

We select the same number of the highest metal stars within the same age period in order to check for biases in the kinematics and origin of low metal stars against high metal stars. Figure 19 shows this selection. Just like low metal stars, all selected high metal stars are found to be kinematically in the disk independently of their origin. Out of these 215 high metal stars, 84 are "in situ" stars and 131 are "gas accreted", with no "star accreted" particles. We therefore find more "gas accreted" high metal stars than low metal stars.

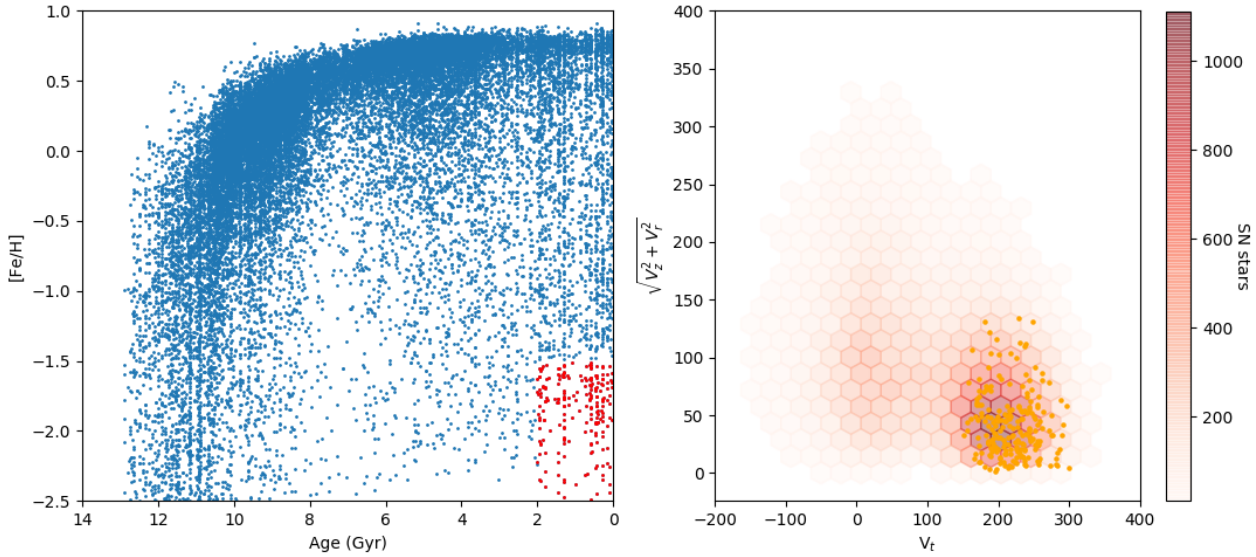

Figure 18: Left: [Fe/H] versus age diagram of stars in the solar neighborhood of galaxy nmdh1. Low metal young tracked stars within the limits of the plot are marked in red. Right: Toomre diagram of stars in the solar neighborhood (SN) of galaxy nmdh1. Low metal young tracked stars are marked by orange points.

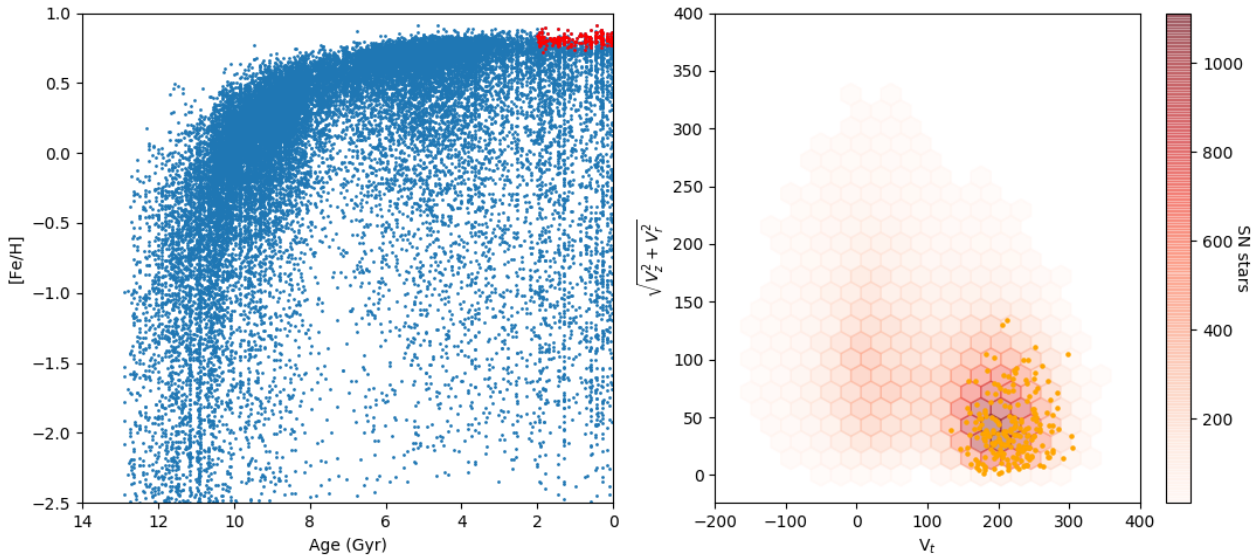

Figure 19: Left: [Fe/H] versus age diagram of stars in the solar neighborhood of galaxy nmdh1. High metal young tracked stars within the limits of the plot are marked in red. Right: Toomre diagram of stars in the solar neighborhood (SN) of galaxy nmdh1. Low metal young tracked stars are marked by orange points.

We also study the elapsed time between the accretion and formation of the selected stars. Figure 20 shows this time interval against the accretion time of both high and low metal stars. We find high metal stars have higher T2-T1 values than low metal stars. Since the formation times of all these stars is similar, this means that high metal stars were accreted earlier than low metal stars. This fact implies that metal enrichment happens mainly in the MW and not earlier in accreted galaxies. This is a natural consequence of lower mass galaxies being less efficient at forming stars that contribute to gas enrichment, as noted by Brook et al. [2020] and depicted by the stellar mass - halo mass relation. Metal enrichment from supernovae and other sources occurs in the simulation although there is no metal diffusion implemented in it.

A noticeable number of ”in situ” high metal stars are accreted from the IGM at late times, so they must have been enriched very quickly inside the MW. Low metal stars are generally accreted later, specially in the case of ”gas accreted” stars. Low metal ”in situ” stars are more spread, and some even have T2-T1 values of around 10 Gyr. These particles have been inside the galaxy for a long time before they formed stars, but they have not been enriched during this lapse of time.

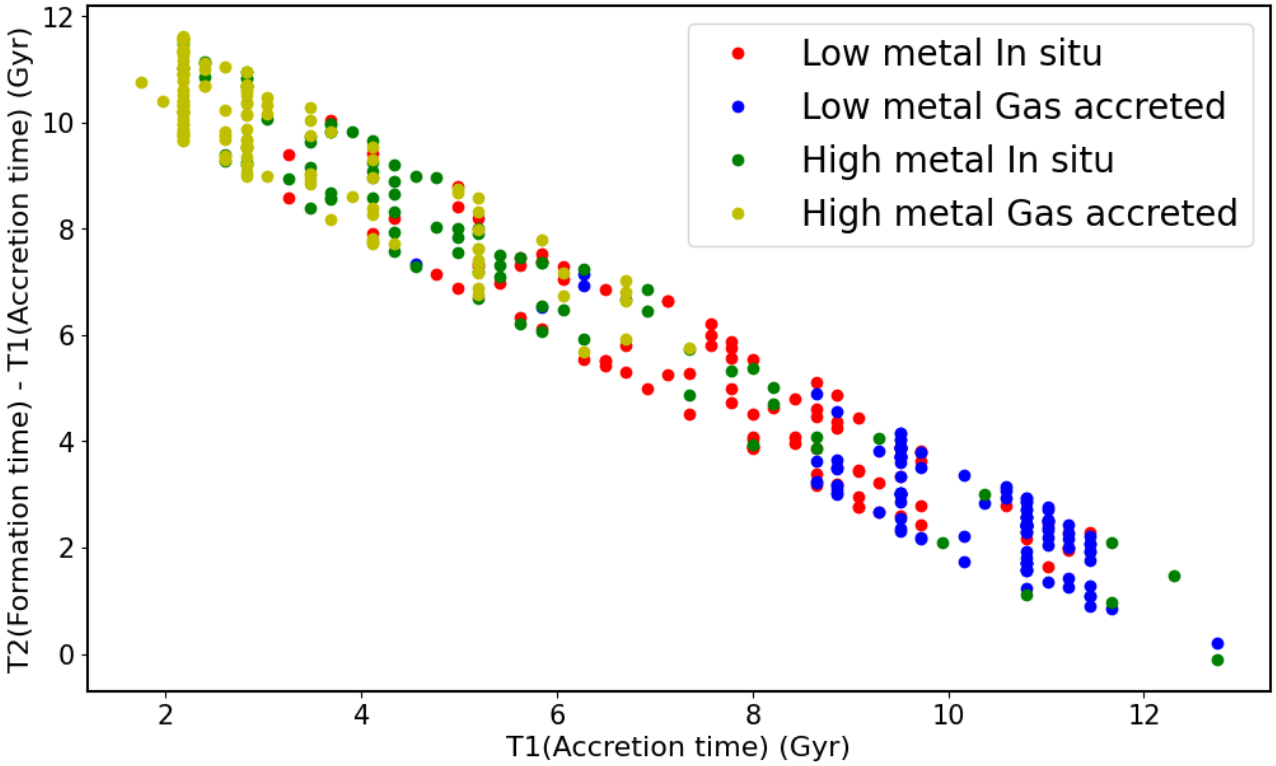

Figure 20: Time elapsed since the approximated instant a tracked particle corresponding to a young star entered the main halo of NIHAO nmdh1 simulation until the time it formed a star. The X-axis shows the accretion time.

We repeat the tracking process with older stars of between 6 and 8 Gyr of age. We again select stars with [Fe/H < -1.5. In this case, the sample size is of 69 stars. We select the same number of stars among those with highest [Fe/H] in the same age range. The selection of low metal and high metal stars are respectively shown in figures 21 and 22. Similarly to young stars, most old stars have disk-like kinematics, although high metal old stars are noticeably more disperse in the Toomre diagram. This continues the discrepancy between the results of the kinematic study in g15784 and nmdh1. In order to solve this it would be necessary to study the individual merger histories of both galaxies, looking for any property of the accretion event that presents correlation with the resulting kinematics of the accreted stars. We find 42 ”in situ” low metal stars and 27 ”gas accreted” low metal stars. Just as we observed for young stars, the number of ”in situ” stars is smaller among high metal stars, it being 21. 48 out of the 69 high metal old stars are labeled as ”gas accreted”. Once again, we find no ”star accreted” particles in the selection. Figure 23 shows the time elapsed since accretion until formation against the accretion time of the old tracked stars. This figure depicts similar information to its analogue for young stars: high metal stars enter the main galaxy earlier than low metal stars and they also form later, ”gas accreted” stars follow this trend more tightly than ”in situ” stars, which present more scatter in the diagram.

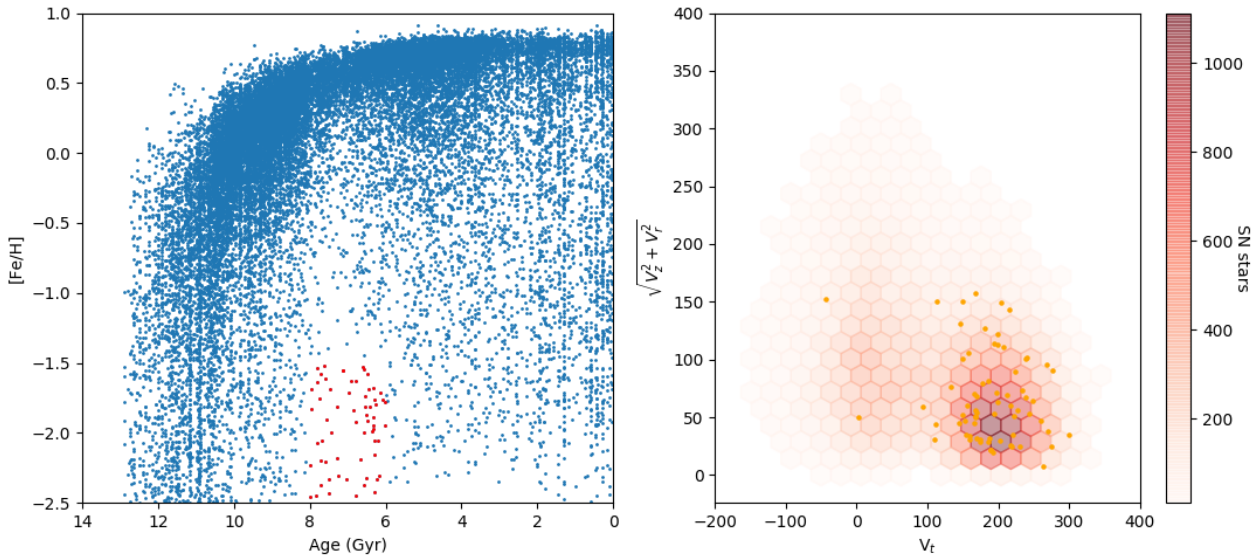

Figure 21: Left: [Fe/H] versus age diagram of stars in the solar neighborhood of galaxy nmdh1. Low metal old tracked stars within the limits of the plot are marked in red. Right: Toomre diagram of stars in the solar neighborhood of galaxy g15784. Low metal young tracked stars are marked by orange points.

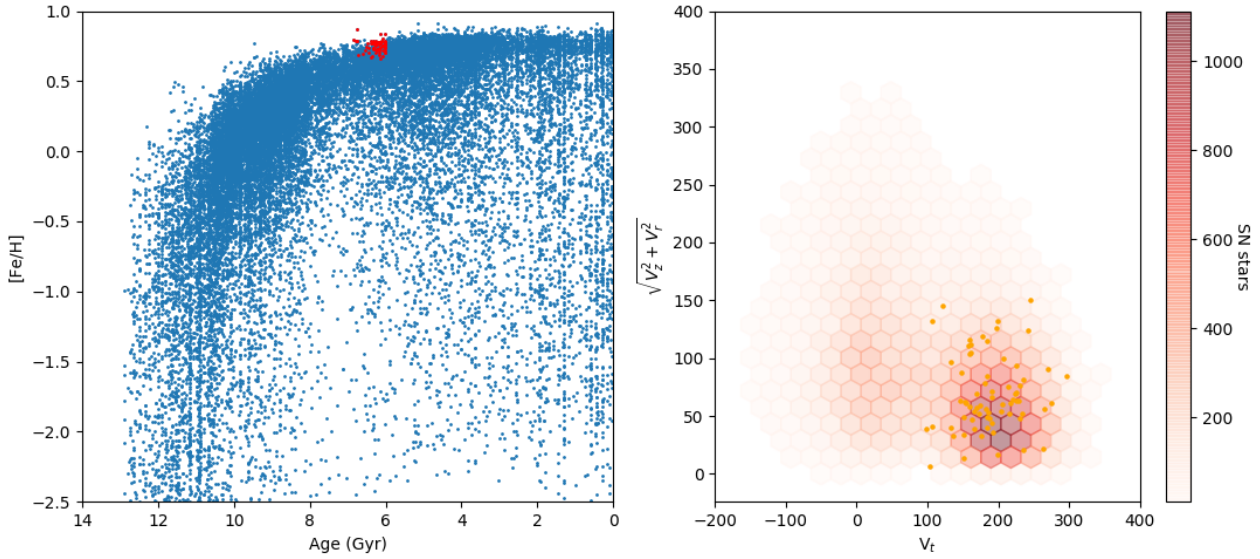

Figure 22: Left: [Fe/H] versus age diagram of stars in the solar neighborhood of galaxy nmdh1. High metal old tracked stars within the limits of the plot are marked in red. Right: Toomre diagram of stars in the solar neighborhood of galaxy g15784. Low metal young tracked stars are marked by orange points.

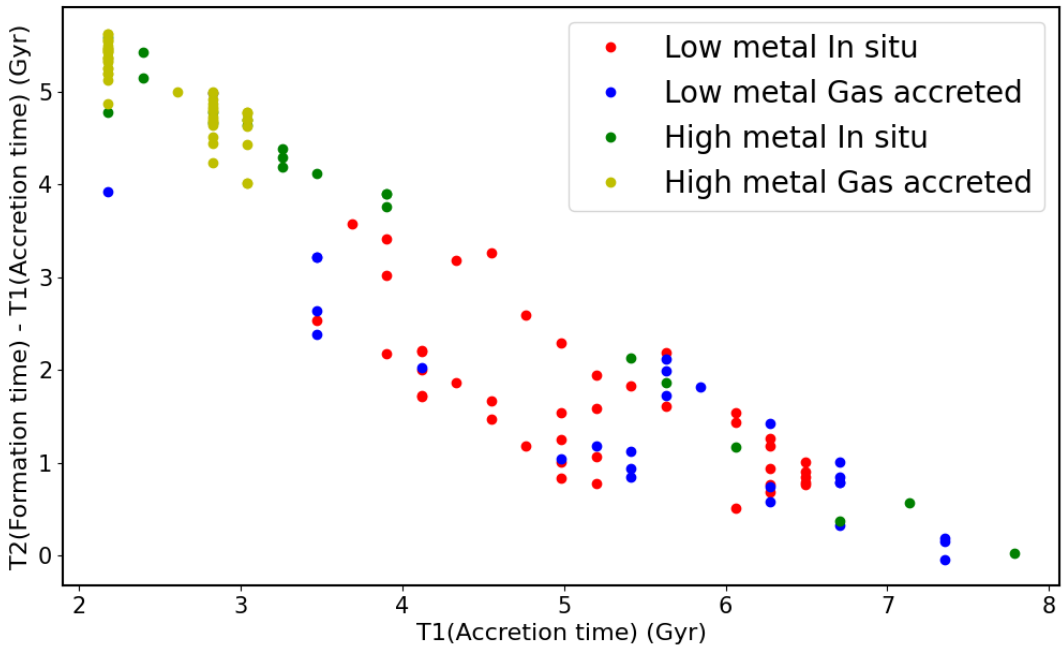

Figure 23: Time elapsed since the approximated instant a tracked particle corresponding to an old star entered the main halo of NIHAO nmdh1 simulation until the time it formed a star. The X-axis shows the accretion time.

6. Conclusions

We have reviewed a set of simulated galaxies with diverse masses, morphologies and simulation methods. All 23 galaxies in the initial sample are extracted from simulations from the projects HESTIA, MAGICC and NIHAO. We select 12 MW-like galaxies with masses between 0.685 and 1.80 $\times$ 10 ^{12} $M_\odot$ and stellar masses between 1.26 and 10.67 $\times$ 10 ^{10} $M_\odot$. Even after reducing the sample by selecting MW-like galaxies, we have found diversity in the general traits of different galaxies. We sum up the general analysis of the sample with the following points:

- The main differences we noticed concerning metal dispersion are the scatter in [Fe/H] versus age diagrams (see figure 7) and in the [O/Fe] versus [Fe/H] space (see figure 9). We find more scatter in simulations with lower metal diffusion rates. The scatter increases in simulations in this order: SPH with no metal diffusion, quasi-lagrangian, SPH with metal diffusion implementations mimicking Eulerian diffusion.
- We also observed the presence of mergers and their visibility in the [Fe/H] versus age diagrams and in the [O/Fe] versus [Fe/H] diagrams, in the form of secondary tracks separated from the main sequence of stars in the diagram.
- Furthermore, we analyze the time and duration of the peak in star formation; and the general shape of the [O/Fe] versus [Fe/H] diagrams. We find that, in order for a simulated galaxy to reproduce the MW's metal distribution (specially in the [O/Fe] versus [Fe/H] space) it must have a similar star formation history to that of the MW, with low and constant recent star formation rates, rather than recent bursts.

- We stress the importance of relying on abundance matching stellar mass - halo mass relations for setting up simulations. Deviations in this aspect have an effect in the metallicity of galaxies accreted in the MW, and they therefore modify the final metal distribution. Element abundances are affected by this mismatch due to their dependence on the presence of type I and II supernovae, which become more abundant in a galaxy with too many stars, and vice versa. We observed this behaviour in HESTIA simulations as shown in figure 8.

More in depth study of MW-like galaxies NIHAO mdh2 (NIHAO SPH simulation with metal diffusion), NIHAO nmdh1 (NIHAO SPH simulation with no metal diffusion), HESTIA 17_11h2 (quasi-Lagrangian simulation) and g15784 (a different SPH simulation with metal diffusion) helped us remark the differences in the results of simulations depending on the strength of their metal diffusion implementation:

- We observe how simulations with stronger metal diffusion have more homogeneous metal distribution both for their stars and gas.
- We see in figure 10 that the [Fe/H] distribution of NIHAO nmdh1's stars in the solar neighborhood is too spread compared with observations and mdh1's distribution is too narrow, whereas HESTIA 17_11h2's data better resembles that of GALAH DR3.
- The [O/Fe] versus [Fe/H] diagrams in figure 12 show that HESTIA 17_11h2's metal diffusion is still too strong to match observations. This is stressed more by the spread area deviations gathered in table 2. From this we conclude the metal diffusion strength a simulation needs to match MW observations is between those of NIHAO nmdh1 and HESTIA.
- Our analysis of simulated LOS observations and subsequent comparison with De Cia et al. [2021]'s observations supports the previous conclusion, as depicted in figure 14 and the rest of panels in the appendix 6: NIHAO nmdh1 presents too much scatter in [Fe/H], whilst the [Fe/H] values of gas in several HESTIA 17_11h2 positions are too homogeneous. This is, accepting De Cia et al. [2021]'s claims of large metallicity variations in the solar neighborhood. However, if Esteban et al. [2022]'s view of a highly uniform metal distribution in the solar neighborhood were more accurate, then the needed metal diffusion strength would be higher. Regardless of this fact, our best guess is still placed somewhere between no diffusion at all and the diffusion implemented in HESTIA. This shows the importance of properly constraining observations in order to be able to use and interpret theoretical models.
- The abundance of low metal stars in the solar neighborhood is also a good indicator for constraining the necessary metal diffusion rate in simulations. As seen in the mid panel of figure 10, having no metal diffusion results in too many low metal stars being found in the solar neighborhood comparing to GALAH data. On the other hand, the upper panel shows that NIHAO's excessive metal diffusion strength leads to a lack of these stars. This is also reflected in the low metal outlier stars in the [Fe/H] versus age diagrams in figure 7. A mid-point like MAGICC, which presents some (but not too many) low metal outliers is probably more representative of the actual MW. We see virtually no outliers in HESTIA panels, presumably due to their mismatch with stellar mass - halo mass relations.
- We found 18 low metal outliers in the [Fe/H] versus age diagram of the solar neihghbourhood of g15784, which is one of the best MW-like simulated galaxies up to this day. After

tracking back their evolution, we determined half of these stars are ”in situ” stars and the other half are ”gas accreted”, but none of them are ”star accreted”. We did not find ”star accreted” stars in the solar neighborhood of galaxy nmdh1 either. This is consistent with the hypothesis that particles being accreted into a galaxy in their star form are unlikely to make it to the solar neighborhood in the disk because of their inability to cool down. We therefore conclude that all the stars we tracked in the solar neighborhood entered the MW-like galaxy in gas form, either from the merger of another galaxy into the main one or directly from the IGM.

- We notice a bias in the kinematics of the two types of tracked stars in g15784: ”gas accreted” stars tend to have halo-like kinematics, whereas ”in situ” stars have disk-like trajectories. Two stars in each category do not agree with the general trend. We studied the time elapsed since the accretion of a tracked particle until it formed a particle, and we found this time interval to be much higher for ”in situ” stars than for ”gas accreted” particles. This means ”in situ” stars spend more time in their gas form inside the galaxy, and they have more opportunities to cool down to the solar neighborhood, explaining the general difference in the kinematics of ”in situ” and ”gas accreted” stars. We also notice three stars that do not follow the general trend of the accretion-formation time of their category. Two of these stars are among the ones that deviate from the trend in terms of kinematics too. This may suggest that the elapsed time since accretion until formation is the main factor for determining the final kinematics of a star. The ”in situ” or ”gas accreted” category of a star does not have a direct effect in its kinematics, but we find a bias for ”in situ” stars to have longer accretion-formation time lapses than ”gas accreted” stars. Since the sample of tracked stars is rather small, these claims should be taken with caution and further proven with larger sets of low metal outliers.
- We also tracked stars in the solar neighborhood of galaxy nmdh1. We selected 215 stars younger than 2 Gyr with [Fe/H]<-1.5 and 69 stars between 6 and 8 Gyr with the same metallicity limit. Then we selected the same number of the highest metallicity stars within the same age ranges. These samples provide more reliable statistics but they are extracted from a simulation with no metal diffusion. We find almost all stars selected from this galaxy to have disk-like kinematics, independently of their accretion category or the time elapsed since their accretion until their formation. This challenges our findings in g15784, and it remains unclear if accretion-formation times are related with the final kinematics of stars. In order to shed light on this question it would be necessary to carefully study the specific merger events where particles entered the simulated galaxies.
- Trough the tracking process in nmdh1 we find a bias for high metal stars against low metal stars to be more likely to enter the MW via accretion events and not directly from the IGM.

References

Oscar Agertz, Ben Moore, Joachim Stadel, Doug Potter, Francesco Miniati, Justin Read, Lucio Mayer, Artur Gawryszczak, Andrey Kravtsov, Åke Nordlund, and et al. Fundamental differ-

ences between sph and grid methods. *Monthly Notices of the Royal Astronomical Society*, 380 (3):963–978, 2007. doi: 10.1111/j.1365-2966.2007.12183.x.

Edward Anders and Nicolas Grevesse. Abundances of the elements: Meteoritic and solar. *Geochimica et Cosmochimica Acta*, 53(1):197–214, 1989. doi: 10.1016/0016-7037(89)90286-x.

Nikhil Arora, Andrea V. Macció, Stéphane Courteau, Tobias Buck, Noam I. Libeskind, Jenny G. Sorce, Chris B. Brook, Yehuda Hoffman, Gustavo Yepes, and Eduardo Carlesi. Nihao-lg: The uniqueness of local group dwarf galaxies. *Monthly Notices of the Royal Astronomical Society*, 2021.

Giuseppina Battaglia, Amina Helmi, Heather Morrison, Paul Harding, Edward W. Olszewski, Mario Mateo, Kenneth C. Freeman, John Norris, and Stephen A. Shectman. The radial velocity dispersion profile of the galactic halo: Constraining the density profile of the dark halo of the milky way. *Monthly Notices of the Royal Astronomical Society*, 364(2):433–442, 2005. doi: 10.1111/j.1365-2966.2005.09367.x.

Edmund Bertschinger. Multiscale gaussian random fields and their application to cosmological simulations. *The Astrophysical Journal Supplement Series*, 137(1):1–20, 2001. doi: 10.1086/322526.

Chris B Brook, Daisuke Kawata, Brad K Gibson, Carme Gallart, and Andrés Vicente. Explaining the chemical trajectories of accreted and in-situ halo stars of the milky way. *Monthly Notices of the Royal Astronomical Society*, 495(3):2645–2651, 2020. doi: 10.1093/mnras/staa992.

Sven Buder, Sanjib Sharma, Janez Kos, Anish M. Amarsi, Thomas Nordlander, Karin Lind, Sarah L. Martell, Martin Asplund, Joss Bland-Hawthorn, Andrew R. Casey, Gayandhi M. de Silva, Valentina D'Orazi, Ken C. Freeman, Michael R. Hayden, Geraint F. Lewis, Jane Lin, Katharine J. Schlesinger, Jeffrey D. Simpson, Dennis Stello, Daniel B. Zucker, Tomaž Zwitter, Kevin L. Beeson, Tobias Buck, Luca Casagrande, Jake T. Clark, Klemen Čotar, Gary S. da Costa, Richard de Grijs, Diane Feuillet, Jonathan Horner, Prajwal R. Kafle, Shourya Khanna, Chiaki Kobayashi, Fan Liu, Benjamin T. Montet, Govind Nandakumar, David M. Nataf, Melissa K. Ness, Lorenzo Spina, Thor Tepper-García, Yuan-Sen Ting, Gregor Traven, Rok Vogrinčič, Robert A. Wittenmyer, Rosemary F. G. Wyse, Maruša Žerjal, and G. A. L. A. H. Collaboration. The galah+ survey: Third data release. *Monthly Notices of the Royal Astronomical Society*, 506: 150–201, 2021. ISSN 0035-8711. doi: 10.1093/mnras/stab1242. URL https://ui.adsabs.harvard.edu/abs/2021MNRAS.506..150B. eprint: arXiv:2011.02505.

Thomas M Callingham, Marius Cautun, Alis J Deason, Carlos S Frenk, Wenting Wang, Facundo A Gó mez, Robert J J Grand, Federico Marinacci, and Ruediger Pakmor. The mass of the milky way from satellite dynamics. *Monthly Notices of the Royal Astronomical Society*, 484(4): 5453–5467, 2019. doi: 10.1093/mnras/stz365. URL https://doi.org/10.1093%2Fmnras%2Fstz365.

Gilles Chabrier. Galactic stellar and substellar initial mass function. *Publications of the Astronomical Society of the Pacific*, 115(809):763–795, 2003. doi: 10.1086/376392.

Annalisa De Cia, Edward B. Jenkins, Andrew J. Fox, Cédric Ledoux, Tanita Ramburuth-Hurt, Christina Konstantopoulou, Patrick Petitjean, and Jens-Kristian Krogager. Large metallicity variations in the galactic interstellar medium. *Nature*, 597(7875):206–208, 2021. doi: 10.1038/s41586-021-03780-0.

K. Dolag, S. Borgani, S. Schindler, A. Diaferio, and A. M. Bykov. Simulation techniques for cosmological simulations. *Space Science Reviews*, 134(1-4):229–268, 2008. doi: 10.1007/s11214-008-9316-5.

Aaron A. Dutton and Andrea V. Macciò. Cold dark matter haloes in the planck era: Evolution of structural parameters for einasto and nfw profiles. *Monthly Notices of the Royal Astronomical Society*, 441(4):3359–3374, 2014. doi: 10.1093/mnras/stu742.

C. Esteban, J. E. Mé ndez-Delgado, J. García-Rojas, and K. Z. Arellano-Córdova. About metallicity variations in the local galactic interstellar medium. *The Astrophysical Journal*, 931(2):92, 2022. doi: 10.3847/1538-4357/ac6b38. URL https://doi.org/10.3847%2F1538-4357%2Fac6b38.

T K Fritz, A Di Cintio, G Battaglia, C Brook, and S Taibi. The mass of our galaxy from satellite proper motions in the gaia era. *Monthly Notices of the Royal Astronomical Society*, 494(4):5178–5193, 2020. doi: 10.1093/mnras/staa1040.

Carme Gallart, Edouard J. Bernard, Chris B. Brook, Tomás Ruiz-Lara, Santi Cassisi, Vanessa Hill, and Matteo Monelli. Uncovering the birth of the milky way through accurate stellar ages with gaia. *Nature Astronomy*, 3(10):932–939, 2019. doi: 10.1038/s41550-019-0829-5.

Stefan Gottlöber, Yehuda Hoffman, and Gustavo Yepes. Constrained local universe simulations (clues). *High Performance Computing in Science and Engineering, Garching/Munich 2009*, page 309–322, 2010. doi: 10.1007/978-3-642-13872-0_26.

Robert J. Grand, Facundo A. Gómez, Federico Marinacci, Rüdiger Pakmor, Volker Springel, David J. Campbell, Carlos S. Frenk, Adrian Jenkins, and Simon D. White. The auriga project: The properties and formation mechanisms of disc galaxies across cosmic time. *Monthly Notices of the Royal Astronomical Society*, 2017. doi: 10.1093/mnras/stx071.

Michael R. Hayden, Jo Bovy, Jon A. Holtzman, David L. Nidever, Jonathan C. Bird, David H. Weinberg, Brett H. Andrews, Steven R. Majewski, Carlos Allende Prieto, Friedrich Anders, Timothy C. Beers, Dmitry Bizyaev, Cristina Chiappini, Katia Cunha, Peter Frinchaboy, D. A. García-Herńandez, Ana E. García Pérez, Léo Girardi, Paul Harding, Fred R. Hearty, Jennifer A. Johnson, Szabolcs Mészáros, Ivan Minchev, Robert O'Connell, Kaike Pan, Annie C. Robin, Ricardo P. Schiavon, Donald P. Schneider, Mathias Schultheis, Matthew Shetrone, Michael Skrutskie, Matthias Steinmetz, Verne Smith, John C. Wilson, Olga Zamora, and Gail Zasowski. Chemical cartography with apogee: Metallicity distribution functions and the chemical structure of the milky way disk. *The Astrophysical Journal*, 808:132, 2015. ISSN 0004-637X. doi: 10.1088/0004-637X/808/2/132. URL https://ui.adsabs.harvard.edu/abs/2015ApJ...808..132H. eprint: arXiv:1503.02110.

Prajwal R. Kafle, Sanjib Sharma, Geraint F. Lewis, and Joss Bland-Hawthorn. Kinematics of the stellar halo and the mass distribution of the milky way using blue horizontal branch stars. *The Astrophysical Journal*, 761(2):98, 2012. doi: 10.1088/0004-637x/761/2/98.

Prajwal Raj Kafle, Sanjib Sharma, Geraint F. Lewis, and Joss Bland-Hawthorn. On the shoulders of giants: Properties of the stellar halo and the milky way mass distribution. *The Astrophysical Journal*, 794(1):59, 2014. doi: 10.1088/0004-637x/794/1/59.

Steffen R. Knollmann and Alexander Knebe. Ahf: Amiga's halo finder. *The Astrophysical Journal Supplement Series*, 182(2):608–624, 2009. doi: 10.1088/0067-0049/182/2/608.

A. V. Kravtsov, A. A. Vikhlinin, and A. V. Meshcheryakov. Stellar mass—halo mass relation and star formation efficiency in high-mass halos. *Astronomy Letters*, 44(1):8–34, 2018. doi: 10.1134/s1063773717120015. URL https://doi.org/10.1134%2Fs1063773717120015.

Noam I Libeskind, Edoardo Carlesi, Robert J Grand, Arman Khalatyan, Alexander Knebe, Ruediger Pakmor, Sergey Pilipenko, Marcel S Pawlowski, Martin Sparre, Elmo Tempel, and et al. The hestia project: Simulations of the local group. *Monthly Notices of the Royal Astronomical Society*, 498(2):2968–2983, 2020. doi: 10.1093/mnras/staa2541.

Timothy C. Licquia and Jeffrey A. Newman. Improved estimates of the milky way's stellar mass and star formation rate from hierarchical bayesian meta-analysis. *The Astrophysical Journal*, 806(1):96, 2015a. doi: 10.1088/0004-637x/806/1/96.

Timothy C. Licquia and Jeffrey A. Newman. IMPROVED ESTIMATES OF THE MILKY WAY's STELLAR MASS AND STAR FORMATION RATE FROM HIERARCHICAL BAYESIAN META-ANALYSIS. *The Astrophysical Journal*, 806(1):96, 2015b. doi: 10.1088/0004-637x/806/1/96. URL https://doi.org/10.1088%2F0004-637x%2F806%2F1%2F96.

Steven R. Majewski, Ricardo P. Schiavon, Peter M. Frinchaboy, Carlos Allende Prieto, Robert Barkhouser, Dmitry Bizyaev, Basil Blank, Sophia Brunner, Adam Burton, Ricardo Carrera, S. Drew Chojnowski, Kátia Cunha, Courtney Epstein, Greg Fitzgerald, Ana E. García Pérez, Fred R. Hearty, Chuck Henderson, Jon A. Holtzman, Jennifer A. Johnson, Charles R. Lam, James E. Lawler, Paul Maseman, Szabolcs Mészáros, Matthew Nelson, Duy Coung Nguyen, David L. Nidever, Marc Pinsonneault, Matthew Shetrone, Stephen Smee, Verne V. Smith, Todd Stolberg, Michael F. Skrutskie, Eric Walker, John C. Wilson, Gail Zasowski, Friedrich Anders, Sarbani Basu, Stephane Beland, Michael R. Blanton, Jo Bovy, Joel R. Brownstein, Joleen Carlberg, William Chaplin, Cristina Chiappini, Daniel J. Eisenstein, Yvonne Elsworth, Diane Feuillet, Scott W. Fleming, Jessica Galbraith-Frew, Rafael A. García, D. Aníbal García-Hernández, Bruce A. Gillespie, Léo Girardi, James E. Gunn, Sten Hasselquist, Michael R. Hayden, Saskia Hekker, Inese Ivans, Karen Kinemuchi, Mark Klaene, Suvrath Mahadevan, Savita Mathur, Benoît Mosser, Demitri Muna, Jeffrey A. Munn, Robert C. Nichol, Robert W. O'Connell, John K. Parejko, A. C. Robin, Helio Rocha-Pinto, Matthias Schultheis, Aldo M. Serenelli, Neville Shane, Victor Silva Aguirre, Jennifer S. Sobeck, Benjamin Thompson, Nicholas W. Troup, David H. Weinberg, and Olga Zamora. The apache point observatory galactic evolution experiment (apogee). *The Astronomical Journal*, 154:94, 2017. ISSN 0004-6256. doi: 10.3847/

1538-3881/aa784d. URL https://ui.adsabs.harvard.edu/abs/2017AJ....154...94M. eprint: arXiv:1509.05420.

Paul J. McMillan. Mass models of the milky way. *Monthly Notices of the Royal Astronomical Society*, 414(3):2446–2457, 2011. doi: 10.1111/j.1365-2966.2011.18564.x.

Paul J. McMillan. The mass distribution and gravitational potential of the milky way. *Monthly Notices of the Royal Astronomical Society*, 465(1):76–94, 2016. doi: 10.1093/mnras/stw2759.

M. S. Miranda, K. Pilkington, B. K. Gibson, C. B. Brook, P. Sánchez-Blázquez, I. Minchev, C. G. Few, R. Smith, R. Domínguez-Tenreiro, A. Obreja, and et al. Origin of the metallicity distribution in the thick disc. *Astronomy & Astrophysics*, 587, 2016. doi: 10.1051/0004-6361/201525789.

Benjamin P. Moster, Thorsten Naab, and Simon D. White. Galactic star formation and accretion histories from matching galaxies to dark matter haloes. *Monthly Notices of the Royal Astronomical Society*, 428(4):3121–3138, 2012. doi: 10.1093/mnras/sts261.

Rüdiger Pakmor, Volker Springel, Andreas Bauer, Philip Mocz, Diego J. Munoz, Sebastian T. Ohlmann, Kevin Schaal, and Chenchong Zhu. Improving the convergence properties of the moving-mesh code arepo. *Monthly Notices of the Royal Astronomical Society*, 455(1): 1134–1143, 2015. doi: 10.1093/mnras/stv2380.

G. Raskin, H. Van Winckel, H. Hensberge, A. Jorissen, H. Lehmann, C. Waelkens, G. Avila, J.-P. De Cuyper, P. Degroote, R. Dubosson, and et al. Hermes: A high-resolution fibre-fed spectrograph for the mercator telescope. *Astronomy & Astrophysics*, 526, 2010. doi: 10.1051/0004-6361/201015435.

Isaiah B Santistevan, Andrew Wetzel, Robyn E Sanderson, Kareem El-Badry, Jenna Samuel, and Claude-André Faucher-Giguère. The origin of metal-poor stars on prograde disc orbits in fire simulations of milky way-mass galaxies. *Monthly Notices of the Royal Astronomical Society*, 505(1):921–938, 2021. doi: 10.1093/mnras/stab1345.

Uros Seljak and Matias Zaldarriaga. A line-of-sight integration approach to cosmic microwave background anisotropies. *The Astrophysical Journal*, 469:437, 1996. doi: 10.1086/177793.

Federico Sestito, Tobias Buck, Else Starkenburg, Nicolas F Martin, Julio F Navarro, Kim A Venn, Aura Obreja, Pascale Jablonka, and Andrea V Macciò. Exploring the origin of low-metallicity stars in milky-way-like galaxies with the nihao-uhd simulations. *Monthly Notices of the Royal Astronomical Society*, 500(3):3750–3762, 2020a. doi: 10.1093/mnras/staa3479.

Federico Sestito, Nicolas F Martin, Else Starkenburg, Anke Arentsen, Rodrigo A Ibata, Nicolas Longeard, Collin Kielty, Kristopher Youakim, Kim A Venn, David S Aguado, Raymond G Carlberg, Jonay I González Hernández, Vanessa Hill, Pascale Jablonka, Georges Kordopatis, Khyati Malhan, Julio F Navarro, Rubén Sánchez-Janssen, Guillame Thomas, Eline Tolstoy, Thomas G Wilson, Pedro A Palicio, Spencer Bialek, Rafael Garcia-Dias, Romain Lucchesi, Pierre North, Yeisson Osorio, Lee R Patrick, and Luis Peralta de Arriba. The pristine survey – x. a large population of low-metallicity stars permeates the galactic disc. *Monthly Notices of the*

Royal Astronomical Society: Letters, 497(1):L7–L12, 2020b. doi: 10.1093/mnrasl/slaa022. URL https://doi.org/10.1093%2Fmnrasl%2Fslaa022.

S. Shen, J. Wadsley, and G. Stinson. The enrichment of the intergalactic medium with adiabatic feedback - i. metal cooling and metal diffusion. *Monthly Notices of the Royal Astronomical Society*, 407(3):1581–1596, 2010. doi: 10.1111/j.1365-2966.2010.17047.x.

O. Snaith, M. Haywood, P. Di Matteo, M. D. Lehnert, F. Combes, D. Katz, and A. Gó mez. Reconstructing the star formation history of the milky way disc(s) from chemical abundances. *Astronomy & Astrophysics*, 578:A87, 2015. doi: 10.1051/0004-6361/201424281. URL https://doi.org/10.1051%2F0004-6361%2F201424281.

D. N. Spergel, R. Bean, O. Dore, M. R. Nolta, C. L. Bennett, J. Dunkley, G. Hinshaw, N. Jarosik, E. Komatsu, L. Page, and et al. Three-year wilkinson microwave anisotropy probe (wmap) observations: Implications for cosmology. *The Astrophysical Journal Supplement Series*, 170 (2):377–408, 2007. doi: 10.1086/513700.

Volker Springel. E pur si muove:galilean-invariant cosmological hydrodynamical simulations on a moving mesh. *Monthly Notices of the Royal Astronomical Society*, 401(2):791–851, 2010. doi: 10.1111/j.1365-2966.2009.15715.x.

G. S. Stinson, J. Bailin, H. Couchman, J. Wadsley, S. Shen, S. Nickerson, C. Brook, and T. Quinn. Cosmological galaxy formation simulations using smoothed particle hydrodynamics. *Monthly Notices of the Royal Astronomical Society*, 408(2):812–826, 2010. doi: 10.1111/j.1365-2966.2010.17187.x.

R. Brent Tully, Hélène M. Courtois, Andrew E. Dolphin, J. Richard Fisher, Philippe Héraudeau, Bradley A. Jacobs, Igor D. Karachentsev, Dmitry Makarov, Lidia Makarova, Sofia Mitronova, and et al. Cosmicflows-2: The data. *The Astronomical Journal*, 146(4):86, 2013. doi: 10.1088/0004-6256/146/4/86.

Kim A. Venn, Mike Irwin, Matthew D. Shetrone, Christopher A. Tout, Vanessa Hill, and Eline Tolstoy. Stellar chemical signatures and hierarchical galaxy formation. *The Astronomical Journal*, 128(3):1177–1195, 2004. doi: 10.1086/422734.

Mark Vogelsberger, Federico Marinacci, Paul Torrey, and Ewald Puchwein. Cosmological simulations of galaxy formation. *Nature Reviews Physics*, 2(1):42–66, 2020. ISSN 2522-5820. doi: 10.1038/s42254-019-0127-2. URL https://doi.org/10.1038/s42254-019-0127-2.

J. W. Wadsley, G. Veeravalli, and H. M. Couchman. On the treatment of entropy mixing in numerical cosmology. *Monthly Notices of the Royal Astronomical Society*, 387(1):427–438, 2008. doi: 10.1111/j.1365-2966.2008.13260.x.

J.W. Wadsley, J. Stadel, and T. Quinn. Gasoline: A flexible, parallel implementation of treesph. *New Astronomy*, 9(2):137–158, 2004. doi: 10.1016/j.newast.2003.08.004.

Liang Wang, Aaron A. Dutton, Gregory S. Stinson, Andrea V. Macciò, Camilla Penzo, Xi Kang, Ben W. Keller, and James Wadsley. Nihao project – i. reproducing the inefficiency of galaxy

formation across cosmic time with a large sample of cosmological hydrodynamical simulations. *Monthly Notices of the Royal Astronomical Society*, 454(1):83–94, 2015. doi: 10.1093/mnras/stv1937.

A. Reproducing LOS observations from other potential Sun locations in simulations.

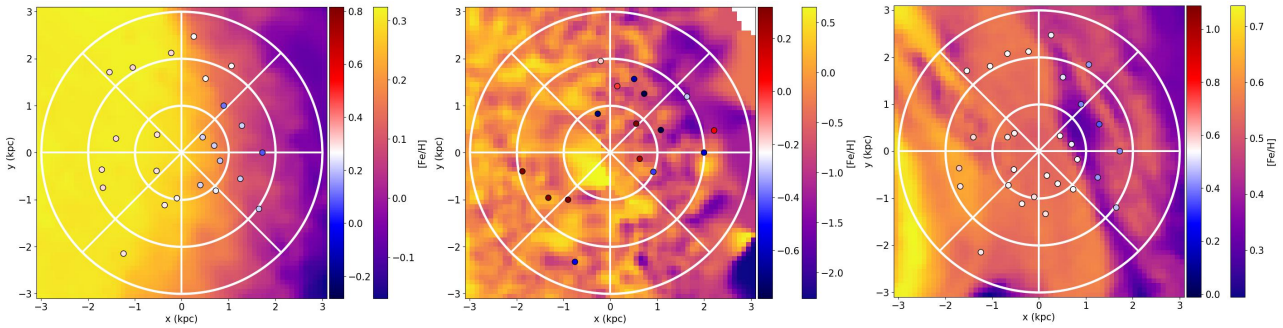

Figure A.1: Zoom-in of potential Sun location 1 marked in the left panels of figure 14. The format of the panels is the same as for those in the right column of figure 14. From leftmost to rightmost panel: NIHAO md, NIHAO nmd, HESTIA 17_11h2.

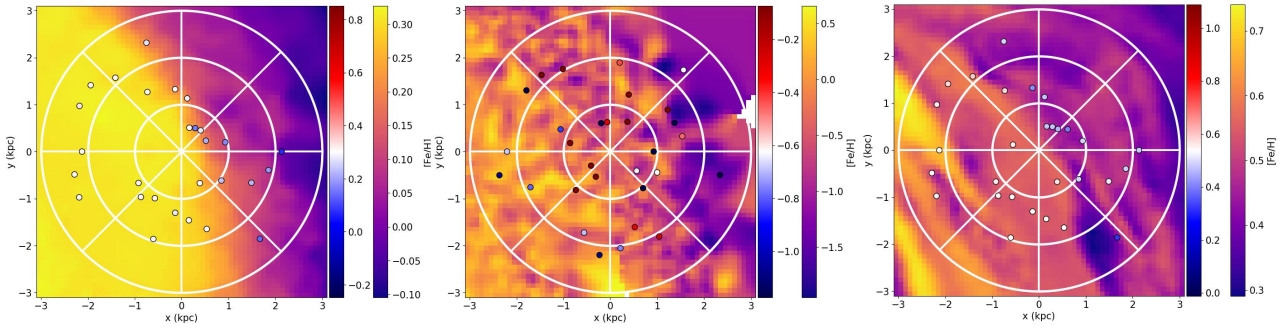

Figure A.2: Zoom-in of potential Sun location 2 marked in the left panels of figure 14. The format of the panels is the same as for those in the right column of figure 14. From leftmost to rightmost panel: NIHAO md, NIHAO nmd, HESTIA 17_11h2.

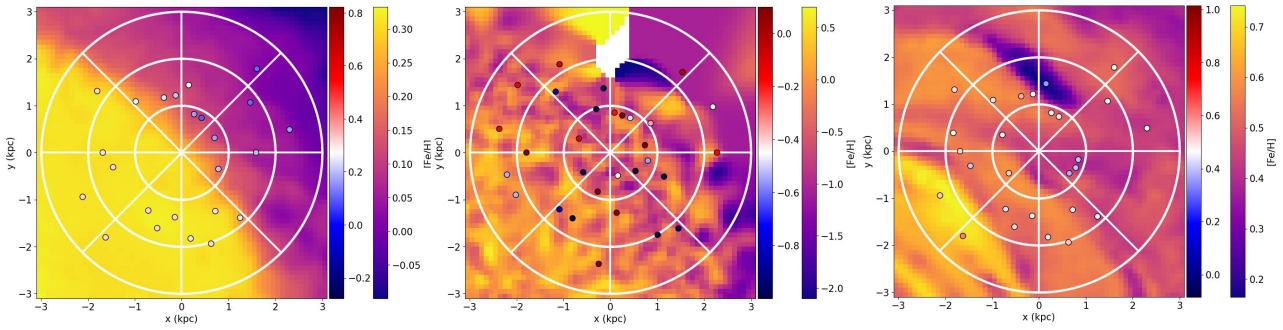

Figure A.3: Zoom-in of potential Sun location 3 marked in the left panels of figure 14. The format of the panels is the same as for those in the right column of figure 14. From leftmost to rightmost panel: NIHAO md, NIHAO nmd, HESTIA 17_11h2.

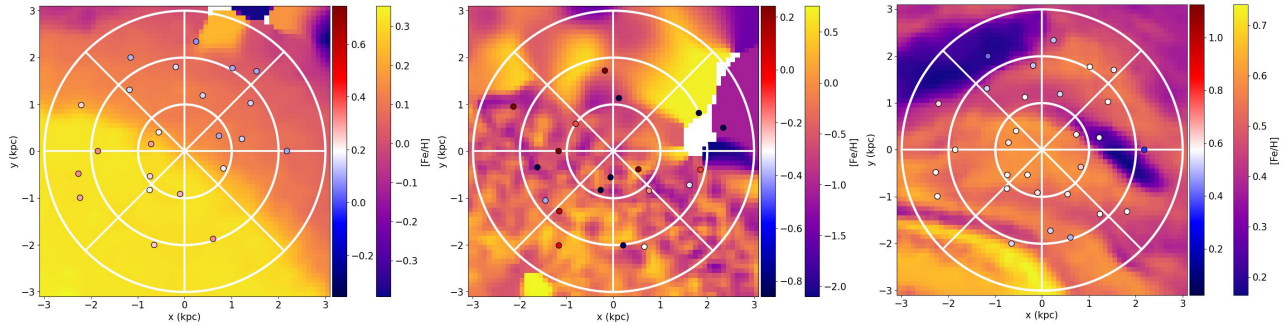

Figure A.4: Zoom-in of potential Sun location 4 marked in the left panels of figure 14. The format of the panels is the same as for those in the right column of figure 14. From leftmost to rightmost panel: NIHAO md, NIHAO nmd, HESTIA 17_11h2.

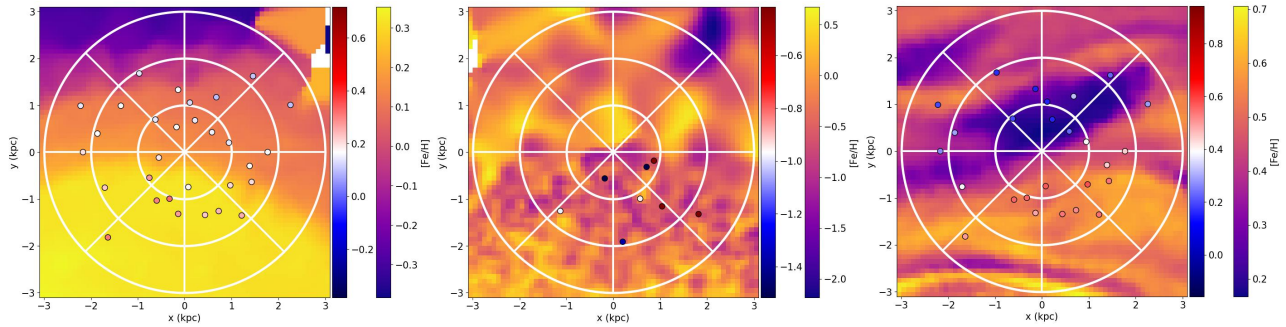

Figure A.5: Zoom-in of potential Sun location 5 marked in the left panels of figure 14. The format of the panels is the same as for those in the right column of figure 14. From leftmost to rightmost panel: NIHAO md, NIHAO nmd, HESTIA 17_11h2.

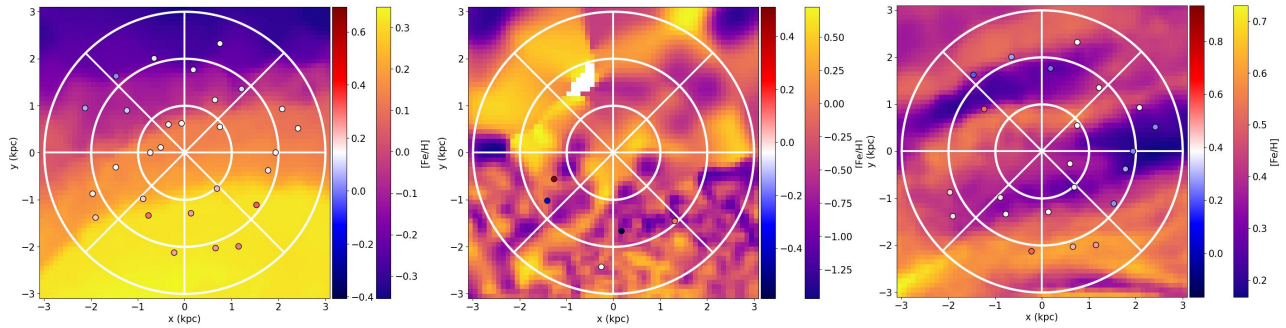

Figure A.6: Zoom-in of potential Sun location 6 marked in the left panels of figure 14. The format of the panels is the same as for those in the right column of figure 14. From leftmost to rightmost panel: NIHAO md, NIHAO nmd, HESTIA 17_11h2.

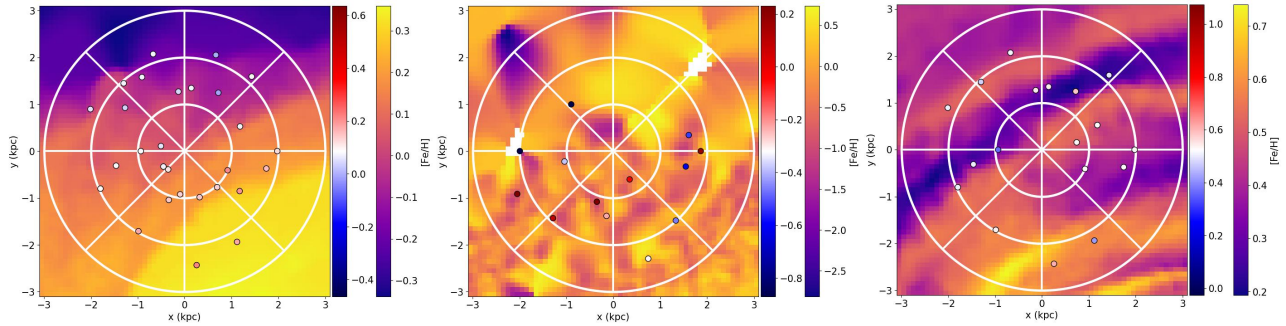

Figure A.7: Zoom-in of potential Sun location 7 marked in the left panels of figure 14. The format of the panels is the same as for those in the right column of figure 14. From leftmost to rightmost panel: NIHAO md, NIHAO nmd, HESTIA 17_11h2.

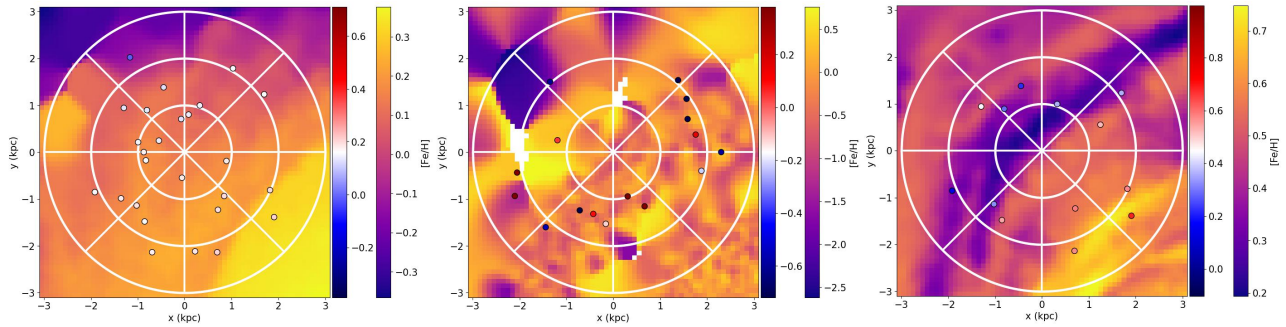

Figure A.8: Zoom-in of potential Sun location 8 marked in the left panels of figure 14. The format of the panels is the same as for those in the right column of figure 14. From leftmost to rightmost panel: NIHAO md, NIHAO nmd, HESTIA 17_11h2.

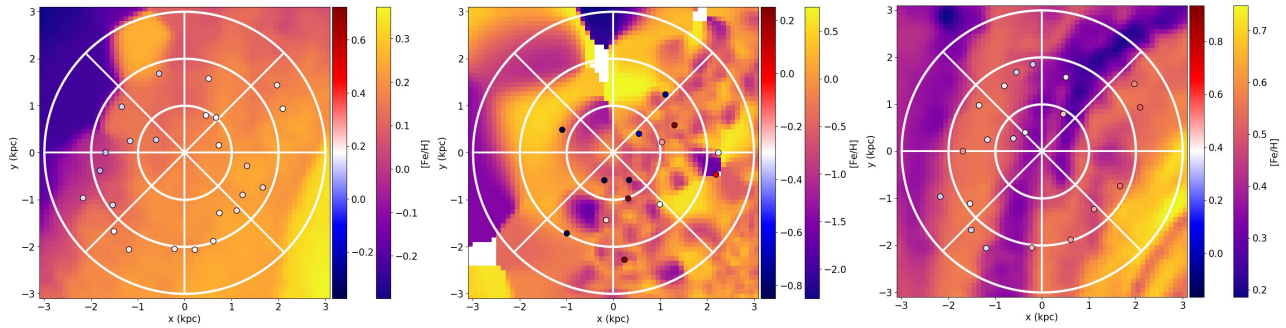

Figure A.9: Zoom-in of potential Sun location 9 marked in the left panels of figure 14. The format of the panels is the same as for those in the right column of figure 14. From leftmost to rightmost panel: NIHAO md, NIHAO nmd, HESTIA 17_11h2.

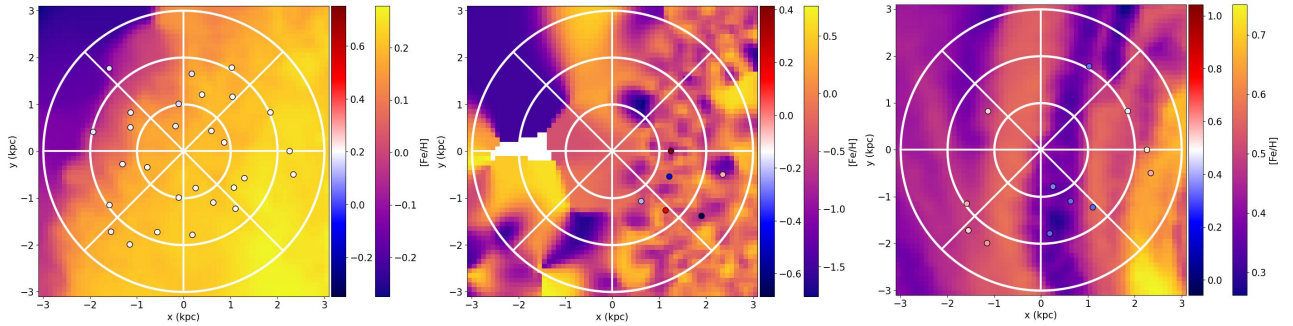

Figure A.10: Zoom-in of potential Sun location 10 marked in the left panels of figure 14. The format of the panels is the same as for those in the right column of figure 14. From leftmost to rightmost panel: NIHAO md, NIHAO nmd, HESTIA 17_11h2.

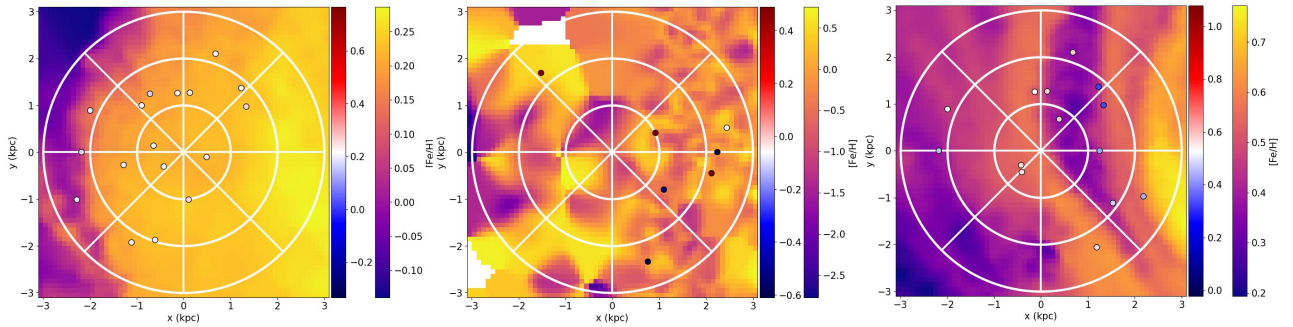

Figure A.11: Zoom-in of potential Sun location 11 marked in the left panels of figure 14. The format of the panels is the same as for those in the right column of figure 14. From leftmost to rightmost panel: NIHAO md, NIHAO nmd, HESTIA 17_11h2.

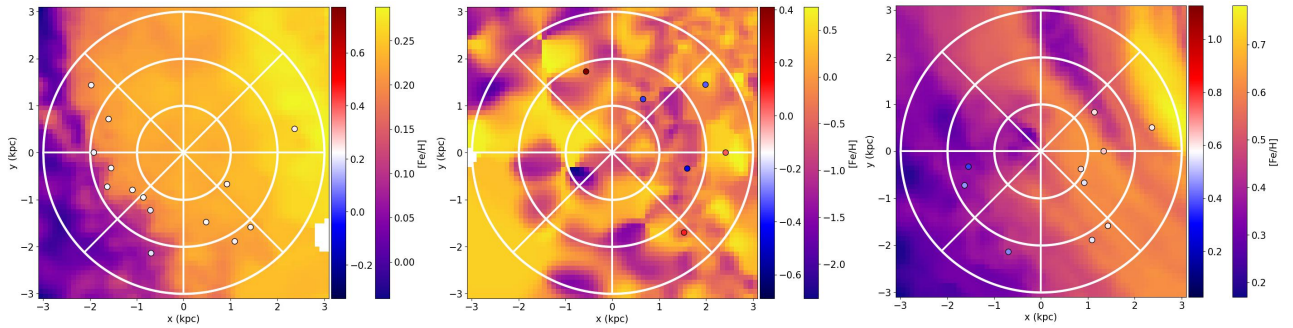

Figure A.12: Zoom-in of potential Sun location 12 marked in the left panels of figure 14. The format of the panels is the same as for those in the right column of figure 14. From leftmost to rightmost panel: NIHAO md, NIHAO nmd, HESTIA 17_11h2.

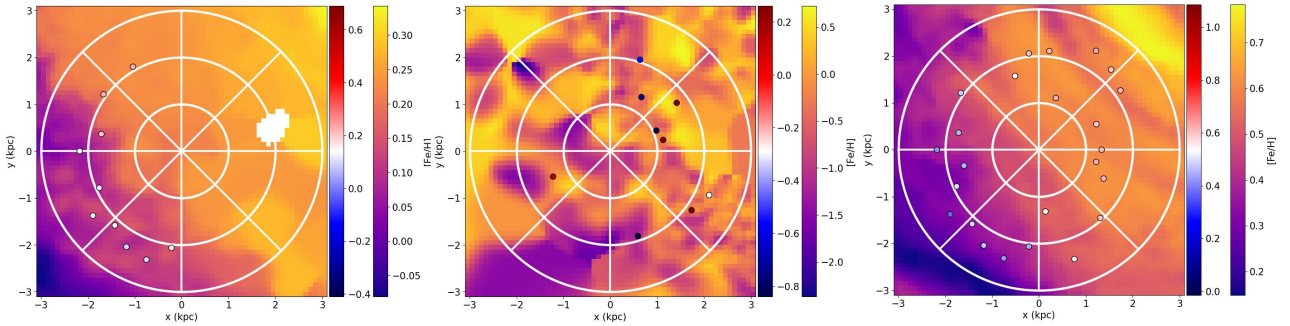

Figure A.13: Zoom-in of potential Sun location 13 marked in the left panels of figure 14. The format of the panels is the same as for those in the right column of figure 14. From leftmost to rightmost panel: NIHAO md, NIHAO nmd, HESTIA 17_11h2.

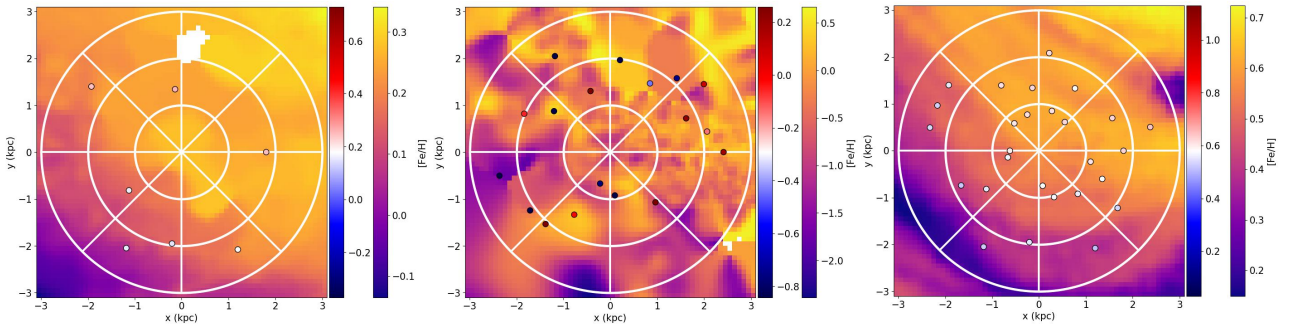

Figure A.14: Zoom-in of potential Sun location 14 marked in the left panels of figure 14. The format of the panels is the same as for those in the right column of figure 14. From leftmost to rightmost panel: NIHAO md, NIHAO nmd, HESTIA 17_11h2.

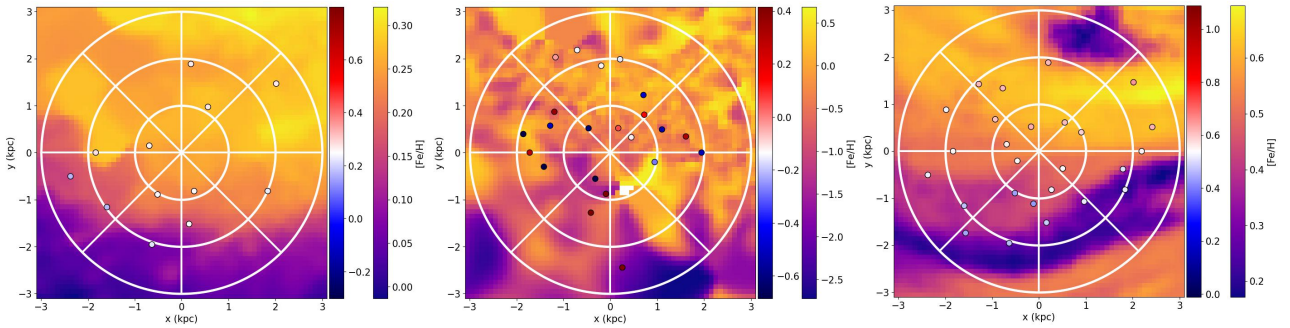

Figure A.15: Zoom-in of potential Sun location 15 marked in the left panels of figure 14. The format of the panels is the same as for those in the right column of figure 14. From leftmost to rightmost panel: NIHAO md, NIHAO nmd, HESTIA 17_11h2.

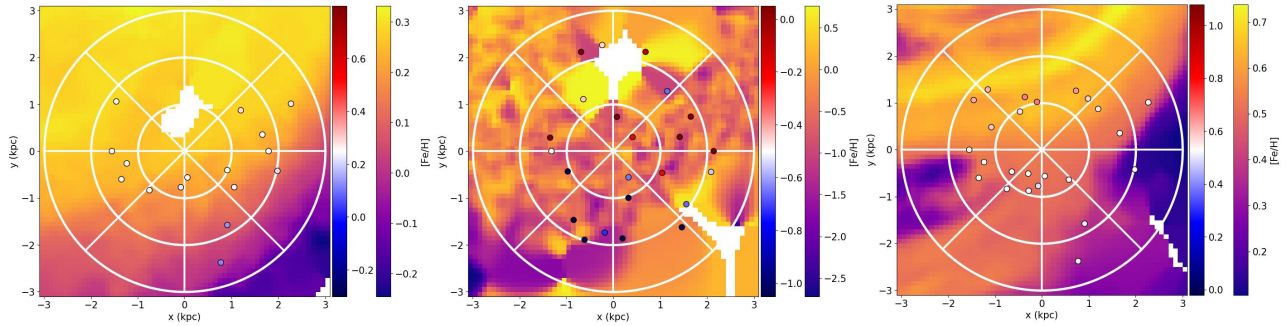

Figure A.16: Zoom-in of potential Sun location 17 marked in the left panels of figure 14. The format of the panels is the same as for those in the right column of figure 14. From leftmost to rightmost panel: NIHAO md, NIHAO nmd, HESTIA 17_11h2.

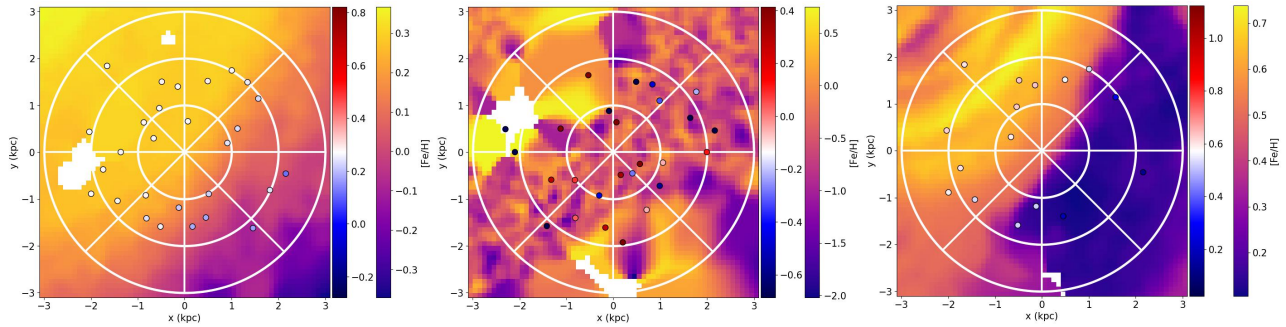

Figure A.17: Zoom-in of potential Sun location 18 marked in the left panels of figure 14. The format of the panels is the same as for those in the right column of figure 14. From leftmost to rightmost panel: NIHAO md, NIHAO nmd, HESTIA 17_11h2.

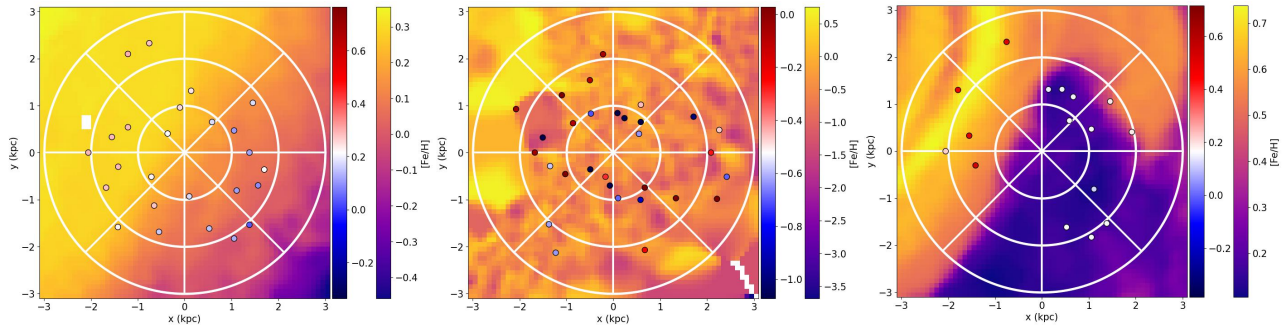

Figure A.18: Zoom-in of potential Sun location 19 marked in the left panels of figure 14. The format of the panels is the same as for those in the right column of figure 14. From leftmost to rightmost panel: NIHAO md, NIHAO nmd, HESTIA 17_11h2.

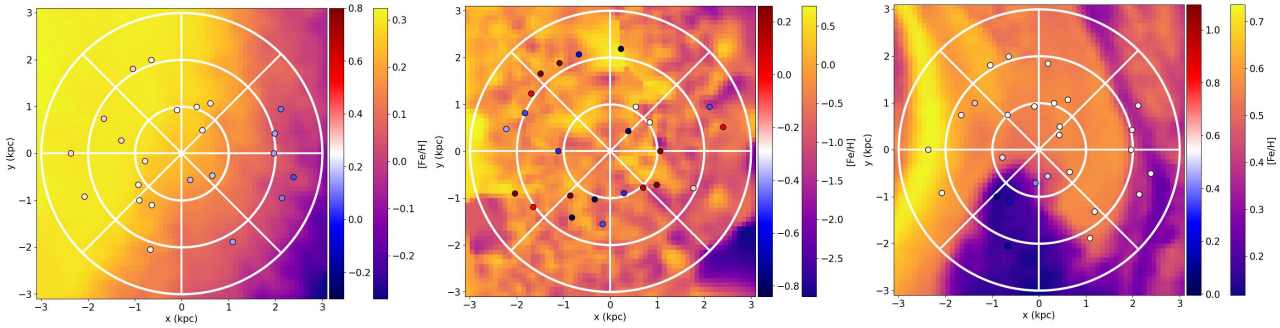

Figure A.19: Zoom-in of potential Sun location 20 marked in the left panels of figure 14. The format of the panels is the same as for those in the right column of figure 14. From leftmost to rightmost panel: NIHAO md, NIHAO nmd, HESTIA 17_11h2.